Chemical Engineering Journal 518 (2025) 164314

Contents lists available at ScienceDirect

Chemical Engineering Journal

journal homepage: www.elsevier.com/locate/cej

Zeolite@Metal-organic framework core-shell synthesized from the aluminum of the zeolite with accessible internal surface for CO_2 adsorption

Lucas Güemes [a,b], Marta Navarro [a,c], Fernando Cacho-Bailo [b,d], Cristian D. Jaimes-Paez [e], Diego Cazorla-Amorós [f], Carlos Téllez [a,b], Joaquín Coronas [a,b,*]

[a] *Instituto de Nanociencia y Materiales de Aragón (INMA), Universidad de Zaragoza-CSIC, 50018 Zaragoza, Spain*
[b] *Departamento de Ingeniería Química y Tecnologías del Medio Ambiente, Universidad de Zaragoza 50018 Zaragoza, Spain*
[c] *Laboratorio de Microscopías Avanzadas, Universidad de Zaragoza 50018 Zaragoza, Spain*
[d] *Industrias Químicas del Ebro S. A. Grupo IQE, 50016 Zaragoza, Spain*
[e] *Instituto Universitario de Materiales de Alicante (IUMA), Universidad de Alicante 03080 Alicante, Spain*
[f] *Departamento de Química Inorgánica, Instituto Universitario de Materiales de Alicante (IUMA), Universidad de Alicante 03080 Alicante, Spain*

ARTICLE INFO

Keywords:
Zeolite 4A
Metal-organic framework
Hybrid material
Core-shell
CO_2 adsorption

ABSTRACT

Combining the rigid microporosity of zeolites with the more versatile structures of metal–organic frameworks (MOFs) seeks to obtain a synergistic effect of both materials. Starting from a low cost and industrially produced zeolite, as it is zeolite NaA (with the LTA type structure), we show that it is possible to crystallize a MOF as shell onto it by only using an aqueous solution of terephthalic acid (H_2BDC). Unlike other zeolite-MOF hybrids reported in the literature, the crystallized MOF only uses the aluminum from the zeolite and may share in turn some aluminum atoms with the inorganic zeolite core, therefore it consists solely of zeolitic Al and BDC. Depending on the pretreatment of the zeolite and the synthesis conditions (pH, time, linker ratio), the crystalline zeolite core is maintained or converted into an amorphous aluminosilicate. Thus, it is possible to retain a part of the adsorption properties of the parent zeolite without degrading its structure. The resulting core–shell material, designated as LTA@Al-BDC, combines the zeolite microporosity and molecular sieving properties with the MOF that crystallizes as high aspect ratio sheets which, together with its hydrophobicity, favors the contact with polymeric materials. In addition, being zeolite 4A (NaA) affinity towards CO_2 been probed, the resulting LTA@Al-BDC material constitutes a prominent candidate towards CO_2 separation.

1. Introduction

Zeolites are generally defined as a class of hydrated microporous aluminosilicates composed of connected TO_4 tetrahedra ($T = Si, Al$), reversibly sorbed water molecules (H_2O), and an exchangeable framework of inorganic cations (mainly alkali or alkali earth metals): $M_{n/m}^{m+}\cdot[Si_{1-n}Al_nO_2]\cdot nH_2O$ [1]. Moreover, zeolites are hierarchically constructed by the interconnexion of different subunits based on the mentioned TO_4 tetrahedra, resulting in the formation of different atomic topologies. The obtained frameworks are defined by their porous structure, whose rigid and well-defined pores have made zeolites known as molecular sieves [2].

Although some zeolites are found in nature and A.F. Cronstedt introduced the term zeolite in 1756 [3], zeolite science golden age started only ca. 90 years ago inspired by the pioneering research carried out by Prof. R. Barrer in the mid-1930s and 1940s [4,5]. So far, the International Zeolite Association (IZA) database has registered 258 unique zeolite framework types using three-letter codes, in which each code groups different zeolite materials that share the same topology [6].

After the blossoming of zeolite science, lately in the 1980s, a new class of crystalline porous solids analogue to zeolites appeared, called metal–organic frameworks (MOF) which have both organic and inorganic character. Their syntheses were further investigated and rationalized, among others, by O.M. Yaghi and co-workers [7,8], who, for the first time, probed the preparation of a stable MOF that retained its porosity in the absence of any guest molecule [9]. MOFs are formed by the connection of inorganic building units (metal ions or clusters) and organic linkers through coordination bonds [10]. An interesting application case study of MOFs appears with water adsorption. Being zeolites one of the most common water adsorbents, they are energy intensive to

---

[*] Corresponding author.
E-mail address: coronas@unizar.es (J. Coronas).

https://doi.org/10.1016/j.cej.2025.164314
Received 24 February 2025; Received in revised form 28 May 2025; Accepted 29 May 2025

regenerate, which has made ultraporous MOFs to be proposed as sorbents for atmospheric water harvesting [11]. Generally, MOFs extend the pore sizes of zeolites and consist of more flexible and versatile structures. Nevertheless, they lack the characteristic thermal, chemical, and structural stability of zeolites.

Given the unique properties of both families of porous materials, there have been several attempts to produce hybrid materials, combining zeolites and MOFs to acquire a synergistic effect of their features (Table 1). For instance, Gao et al. [12] crystallized zeolitic imidazolate framework-8 (ZIF-8) MOF employing zeolite 5A as substrate. They added the ZIF-8 precursors to the zeolite dispersion and, through zeolite silanol-Zn^{2+} interactions, achieved the formation of a ZIF-8 shell. In the same way, Yang et al. [13] reported the formation of a core–shell between zeolite 13X and ZIF-8. In both cases, a hybrid core–shell material was obtained, combining the CO_2 adsorption properties of zeolites 5A and 13X, respectively, with the hydrophobicity of ZIF-8, hence, leading to a prominent adsorbent for CO_2 capture in the presence of water. Following this trend, Choi et al. [14] prepared a core–shell comprised as well by a zeolite 5A core and a ZIF-8 shell. In this case, initially, they exchanged zeolite extraframework ions with Zn^{2+}, for its further conversion into ZnO nanowhiskers, which were subsequently transformed into ZIF-8 in the presence of 2-methylimidazolate linker. The resulting material enhanced the compatibility of the pristine zeolite within an organic polymeric matrix, which allowed to produce a high-performance mixed-matrix-membrane (MMM) for CO_2/CH_4 separation. Zhang et al. [15] coated K-exchanged chabazite zeolite with ZIF-8, obtaining an hydrophobic material that retained the adsorption performance of the former towards CH_4/N_2 separation. But apart from ZIF-8, there are more MOFs that have been as well synthesized onto the surface of zeolite particles to produce hybrid materials: MOF-74 onto zeolite 5A [16,17], UiO-66-NH_2 onto ZSM-5 [18], UiO-66 onto zeolite 4A [19], or MOF-199 onto zeolite ZSM-5 [20]. And beyond gas phase, zeolite@MOFs have also been tested for liquid phase applications such as adsorption [21] and catalysis [22].

It should be noted that in no previous example have the metals of the zeolitic structure been used as reagents for the growth of the MOF. To produce all these materials, an organic ligand and a metallic source were added into a zeolite dispersion, the presence of the latter being limited to act as substrate for MOF crystallization. Differently to these cases, the patent ES 2682056 (EP 3595808), registered by some of the authors of our group, reported the possibility of employing low silica zeolites as aluminum source and substrate at the same time for the growth of an aluminum-based MOF [23,24]. Rani et al. [25] reported as well an aluminum-based MOF growth surrogated to the presence of extra-framework aluminum species in the core zeolites.

In this context, herein we rationalize and study the synthesis of a core–shell porous hybrid material in which zeolite 4A (framework type LTA) serves as a substrate and aluminum source at the same time for the synthesis of an aluminum benzenedicarboxylate (BDC) based MOF. Therefore, the synthesis does not require any other external metal source than the aluminum from the zeolite, and the crystallized MOF shell grows as high aspect ratio sheets. It will be proven that it is essential to control the synthesis conditions (pH, time, BDC concentration, previous calcination of the zeolite) to preserve the porous structure of the zeolite. A battery of characterization techniques (PXRD, TGA, FTIR, SEM, TEM and MAS solid-state NMR) allows to unravel this process in detail in search of the optimal conditions. As will be shown, this approach has some singularities: i) the zeolite provides at the same time the metal source and a substrate in which the MOF crystallizes, leading to a more intimate contact between the zeolite and MOF, ii) the MOF growth is surrogated to the metal leaching from the zeolite, and iii) the synthesis is simple and only requires from H_2BDC, water and NaOH as deprotonator. In addition, the adsorption capacity and porosity of the material have been studied using sorption isotherms with CO_2, N_2 and H_2. Moreover, time-dependent experiments have been carried out to determine the kinetics of CO_2 adsorption and water uptake to determine the hydrophilic/hydrophobic character of the materials and potential compatibility with membrane polymers. Calculations have also been carried out according to the Ideal Adsorbed Solution Theory (IAST) to see the potential of these materials in the separation of CO_2 in post-combustion.

Table 1
Zeolite-MOF hybrid materials.

Hybrid	Hybridizing material		Application	Reference
	Core	Shell		
5A@ZIF-8	Zeolite 5A (LTA)	ZIF-8	CO_2 capture in presence of water	[12]
LiX@ZIF-8	Zeolite 13X (FAU)	ZIF-8	CO_2 capture in presence of water	[13]
CaA@ZIF-8	Zeolite 5A (LTA)	ZIF-8	MMM filler for CO_2/CH_4 separation	[14]
KCHA@ZIF-8	Chabazite-K (CHA)	ZIF-8	Adsorbent for CH_4/N_2 separation	[15]
Zeo-5A@MOF-74	Zeolite 5A (LTA)	MOF-74	Adsorbent for H_2 purification	[16,17]
HZSM-5@UiO-66-NH_2	ZSM-5 (MFI)	UiO-66	Selective catalyzed CO_2 conversion	[18]
LTA@UiO-66	Zeolite 4A (LTA)	UiO-66	MMM filler for O_2/N_2 and CO_2/CH_4 separations	[19]
ZSM-5@MOF-199	ZSM-5 (MFI)	MOF-199	Adsorbent for CO/CO_2 separation	[20]
13X@Zn/Cu-BTC	Zeolite 13X (FAU)	Zn/Cu-BTC	Removal of organic pollutants	[21]
13X@MOF-5	Zeolite 13X (FAU)	MOF-5	Removal of organic pollutants	[21]
13X@ZIF-8	Zeolite 13X (FAU)	ZIF-8	Removal of organic pollutants	[21]
13X@UiO-66	Zeolite 13X (FAU)	UiO-66	Removal of organic pollutants	[21]
ZSM-5@UiO-66	ZSM-5 (MFI)	UiO-66	Bifunctional acid-base catalyst	[22]

2. Experimental section

2.1. Materials

Zeolite 4A (Z4A IQE, NaA, Si/Al = 1) was provided in powder form by Industrias Químicas del Ebro S. A. Spain. Terephthalic acid (1,4-benzenedicarboxylic acid, 98 %) was purchased in powder form from Sigma Aldrich and sodium hydroxide (NaOH, 99 %) was acquired from Scharlab. Dimethyl sulfoxide (DMSO) was obtained from Carlo Erba, while ethanol (EtOH) and water (H_2O) were received from Productos Gilca S.C.

2.2. Synthesis of LTA@Al-BDC

Zeolite 4A was placed into a round-bottom flask, subsequently mixed with water following a molar Al to H_2O ratio of 1:100, and bath-sonicated for 10 min. Then, the desired amount of terephthalic acid (H_2BDC) was added (BDC:Al from 1:2 to 1:6), and the reaction mixture was heated at 35 °C under continuous stirring for the desired time (1 h to 72 h). The white solid obtained was filtered and rinsed with DMSO and lastly with EtOH. Finally, the collected powder was activated at 350 °C for 1 h ($1\ ^\circ C\cdot min^{-1}$). In some cases, prior MOF synthesis, zeolite 4A was calcined at 500 °C for 4 h ($1\ ^\circ C\cdot min^{-1}$).

For the synthesis of LTA@Al-BDC, in which pH was adjusted, H_2BDC and water were placed into a round-bottom flask following a molar BDC to H_2O ratio of 1:200. Then, under continuous stirring, an aqueous solution of NaOH (10 M) was slowly added until the pH was adjusted to the desired value (3.9 to 12.4). Afterwards, zeolite 4A was added (BDC:Al equal to 1:2) and the reaction mixture was heated at 35 °C under continuous stirring for 72 h. The white solid obtained was equally filtered, rinsed and activated as before. All experiments and synthesis conditions used to optimize the LTA@Al-BDC preparation are shown in

Table 2
Relevant synthesis conditions and selected parameters of LTA@Al-BDC samples.

Entry #	Parameter	Al/ BDC	pH*	Time (h)	Shell Yield[a] (%)	a[b] (Å)	I_{LTA} / I_{Shell}[c]
1	Ligand ratio	2	11.0 / 5.6	72	13.9	–	0
2		3	11.0 / 5.8	72	7.3	25.13	0.6
3		4	11.0 / 6.2	72	5.6	24.67	1.9
4		5	11.0 / 6.3	72	4.3	24.58	4.1
5		6	11.0 / 6.7	72	4.1	24.55	12.4
6	Synthesis time	2	11.0 / 5.6	1	3.3	24.51	–
7		2	11.0 / 5.6	2	3.6	24.41	–
8		2	11.0 / 5.6	8	4.3	24.53	5.5
9		2	11.0 / 5.6	12	4.6	24.60	3.0
10		2	11.0 / 5.6	24	7.6	–	0
11		2	11.0 / 5.6	48	9.1	–	0
1	Ligand pH_0	2	3.9 / 5.6	72	13.9	–	0
12		2	5.1 / 5.6	72	11.0	24.61	0.19
13		2	5.7 / 5.8	72	8.4	24.53	13.9
14		2	6.3 / 6.9	72	6.1	24.43	35.3
15		2	9.7 / 7.1	72	–	24.48	–
16	Calcined zeolite	2	11.0 / 5.6	72	15.4	24.43	0.9
17		2	11.0 / 5.6	48	7.4	24.42	5.9
18		2	11.0 / 5.6	24	6.8	24.43	6.2

[*] First pH value is referred to the value measured in the aqueous zeolite dispersion (pH 11), or after the neutralization of the oversaturated BDC solution (pH 3.9–9.7). The second pH was measured at the beginning of the reaction, once all reagents were added, and remained almost unchanged at the end of the synthesis.

[a] Shell percentage was calculated according to equation S1.

[b] Lattice parameters were calculated according to eqs. S2 and S3.

[c] Ratio of PXRD diffractions referred to the LTA plane (200) and shell plane (011) (**Table S1**).

Table 2.

2.3. Characterization of materials

Thermogravimetric analysis (TGA) was carried out in a Mettler Toledo TGA/STDA 851e. A small amount of powder was taken and placed in a 70 μL alumina crucible and subsequently heated from 35 °C to 700 °C. Experiments were performed under a synthetic air atmosphere (15 cm^3 (STP)·min^{-1}). TGA was conducted in two different ways. To assess the hydrophilic behavior and shell formation, a single dynamic segment was set at a heating rate of 10 °C·min^{-1} up to 700 °C; whereas to set a comparison regarding shell formation, samples were first heated to 200 °C at a heating rate of 20 °C·min^{-1}, then the temperature was maintained for 1 h and, finally, temperature was raised to 700 °C at a heating rate of 10 °C·min^{-1}. Field-emission scanning electron microscopy (FE-SEM) images were obtained using an Inspect F50 model (FEI, operated at 10 kV) coupled with an energy-dispersive X-ray (EDX) detector that allowed chemical analysis. Samples were fixed onto carbon tape and coated with Pd. Powder X-ray diffraction (PXRD) patterns were collected in a PANalytical Empyrean-Multipurpose (CuK_{α}) employing a reflection-transmission spinner stage with a zero-background sample holder. The diffraction patterns were acquired in Bragg-Brentano configuration, in the range of 2θ = 5-40°. Fourier transform infrared spectroscopy (FTIR) analysis were conducted in a Bruker Vertex 70 spectrometer equipped with a DTGS detector and a Golden Gate diamond attenuated total reflectance (ATR). Spectra were recorded in the 4000–600 cm^{-1} wavenumber range. Electron probe microanalyzer (EPMA) measurements were performed using a JEOL JXA-iHP200F electron microprobe. Powder samples were embedded in an epoxy resin, then polished and finally carbon coated. Transmission electron microscopy (TEM) and selected area electron diffraction (SAED) were performed using a Tecnai T20 microscope (Thermo Fisher Scientific) operated at 200 keV. Energy dispersive X-ray spectroscopy (EDS) analysis and high angle annular dark field scanning TEM (STEM-HAADF) were performed on a Tecnai G2-F30 field emission gun microscope (Thermo Fisher Scientific) operated at 300 kV. EDX mappings were acquired with an EDS Oxford Instruments Ultim Max TLE 100 detector, installed in an aberration-corrected XFEG TITAN electron microscope (Thermofisher), operated at 300 kV and equipped with a CETCOR Cs-probe corrector from CEOS GmbH (Heidelberg, Germany). Samples were prepared by two means depending on the information needed. For SAED, TEM, STEM and EDS analysis, a drop of particles dispersed in absolute ethanol was placed onto a carbon coated 200 mesh copper grid. For EDX mapping a flat and even surface was more desirable and LTA@Al-BDC samples were embedded in the epoxy resin EMbed 812 at 60 °C for 72 h. After epoxy polymerization, the sample was ultrathin sectioned, using an ultramicrotome Leica EM UC7, to slices of 70 nm in thickness, directly deposited over a carbon coated 200 mesh copper grid. Solid-state high-power decoupling with magic angle spinning (HPDec-MAS) and cross-polarization with magic angle spinning (CP-MAS) nuclear magnetic resonance (NMR) measurements were carried out on a 400 MHz Bruker Avance spectrometer equipped with a 4 mm-wide bore double resonance HX CP-MAS probe. ^{27}Al HPDec-MAS spectra were recorded with a MAS frequency (υMAS) of 12 kHz, applying 1D one-pulse HPDec sequence, using a 0.88 μs excitation pulse, 1.5 s of recycle delay and 4096 scans. ^{29}Si CP-MAS spectra were recorded with a υMAS of 5 kHz, applying CP pulses of 4.3 μs, a 25 s recycle delay and 700 scans.

2.4. Adsorption measurements

To characterize the textural properties, N_2 adsorption–desorption isotherms were measured at −196 °C up to 100 kPa in a Micromeritics TriStar 3000. All samples were previously de-gassed in two steps in a Micromeritics VacPrep^{TM}: initially at 100 °C for 1 h (10 °C·min^{-1}) and then at 200 °C for 10 h (10 °C·min^{-1}). CO_2 adsorption–desorption isotherms were measured at 0 °C up to 100 kPa in a Micromeritics ASAP 2020, all samples were previously de-gassed at 200 °C for 8 h (10 °C·min^{-1}). Moreover, to perform CO_2/N_2 selectivity calculations according to the Ideal Adsorbed Solution Theory (IAST), N_2 adsorption isotherms were also recorded at 0 °C in the same system following a similar procedure as for the CO_2 measurements. IAST calculations were performed employing MicroActive V6 software from Micromeritics. Further details regarding IAST are provided in the Supporting Information.

CO_2 adsorption isotherms at 25 °C up to 100 kPa were measured employing an automatic adsorption equipment, Anton Paar NOVA 800. All samples were previously de-gassed under vacuum at 200 °C for 8 h.

Excess adsorption isotherms for H_2 at high pressures were done at 25 °C up to 8000 kPa using a high-pressure volumetric equipment, iSorb-HP1 equipment from Anton Paar. The temperature of the manifold was maintained constant at 45 °C and the temperature of cell was kept at 25 °C. The volume of the manifold was calibrated using a standard volume carrying out He isotherms. Preliminary tests were performed to ensure that the leak rate was lower than 10^{-6} bar·s^{-1}. The H_2 bulk gas calculations were done using the equation of state of Modified-Benedic-Webb-Rubin [26] and the cell volume was obtained using He at 45 °C. All samples were degassed at 200 °C under vacuum for 8 h. The kinetics of CO_2 adsorption were followed at 25 °C using the same equipment, upon degassing at 200 °C under vacuum for 8 h. Three different equilibrium pressures within the low-pressure region were employed. The kinetic data was analyzed applying a pseudo-second order kinetic model [27].

For the water uptake, samples were kept in a climate chamber, Memmert HPP108, at 20 °C and 50 % relative humidity. Prior analysis, 2 g of sample were dried at 350 °C for 12 h. Mass gain due to water uptake was measured after 24 h and 48 h.

3. Results and discussion

3.1. LTA@Al-BDC synthesis

3.1.1. Influence of Al/BDC molar ratio

The procedure for the synthesis of the core–shell structure starts exposing the zeolite core to an acidic media (terephthalic acid $pK_{a1} = 3.5$ and $pK_{a2} = 4.5$) in which low-silica zeolites such as zeolite A are unstable [4]. Typically, under acid conditions aluminum is leached from zeolite structures through the hydrolysis of Al-O bonds followed by the ion exchange of lattice cations by protons [27]. Nevertheless, zeolite A with a Si:Al molar ratio of 1 does not exist in the H-form, leading to structural collapse and further amorphization [28]. Controlling the amount of H_2BDC seeks to preserve the inner zeolite core and at the same time enable the release of aluminum to allow the MOF-like shell structure to crystallize. Initially, raw zeolite particles were well-defined with cubic shapes, whose size was around 2 μm (Fig. 1a and **S1**). Fig. 1 shows that gradually MOF sheets were developed covering the zeolite particles, increasing their occurrence as the Al/BDC ratio decreases.

The crystallization of the shell material resulted in the appearance of diffraction peaks, at ca. 2θ 8.1° and, in some cases, at ca. 16.2° and 18.0° (Fig. 2a). Compared to the PXRD of Al-based MOFs that include BDC as linker (i.e., MIL-53(Al), CAU-3, MIL-68(Al) and MIL-101(Al) [29]) the obtained pattern is closer to the one exhibited by the high temperature (ht) phase of MIL-53(Al) [30], in which the most intense diffractions appear at ca. 2θ 8.8° (011) and 17.6° (022) (**Fig. S2 and S3**). Considering the same planes for the LTA@Al-BDC, the d-spacing of the most prominent peak (011) is ca. 10.9 Å, matching with the interplanar spacing expected for the same plane in the simulated PXRD of MIL-53 $(Al)_{ht}$. This distance can be related to the MOF interatomic Al-Al distances, which in turn are in the range of certain zeolite LTA Al-Al distances (**Fig. S4**), suggesting that some surface zeolite Al atoms could be shared between the MOF and the zeolite core. Although it cannot be affirmed that the MOF structure corresponds to MIL-53(Al), as it will be shown, there are some important similarities.

The PXRD tendency of Fig. 2a agrees with the crystal sheet development observed by SEM (Fig. 1): as the amount of BDC increases, the diffraction peaks relative to the MOF grow in intensity. Interestingly, although BDC equivalents were correlated to the total zeolite aluminum instead of limiting them to superficial aluminum, in some cases MOF diffraction peaks are barely observed. Besides, Fig. 2a reveals that at Al:BDC < 4 the chemical attack over the zeolite, due to the acidic conditions induced by the dicarboxylic acid, was very efficient and the zeolitic core was not maintained. These findings evidence that there is a compromise between the formation of the MOF shell and the zeolite amorphization.

TGA allows to identify the more thermolabile MOF phase as the weight loss that occurs at ca. 400–700 °C (Fig. 2c). As expected, the weight loss related to the MOF shell increases while the Al/BDC ratio decreases, indicating a major MOF growth in the sample with the lowest Al/BDC ratio. Moreover, thermal analysis points as well to a phase competition between the MOF growth and zeolite amorphization, since the characteristic zeolite weight loss due to adsorbed water (ca. 35–150 °C, Fig. 2d) decreases contrary to MOF formation. Only at an Al/BDC ratio of 6 and for the parent zeolite 4A, clear losses of water appear at low temperature, being limited to less than 2 % for the LTA@Al-BDC syntheses with the Al/BDC ratio in the 2–5 range.

Crystallization of BDC molecules with aluminum atoms from the zeolite is also corroborated by FTIR analysis (Fig. 2b). Some aromatic stretching bands ($C_{sp2}{=}C_{sp2}$) in the range of 1400–1600 cm^{-1} are preserved from pure H_2BDC, while the carbonyl band around 1650 cm^{-1}

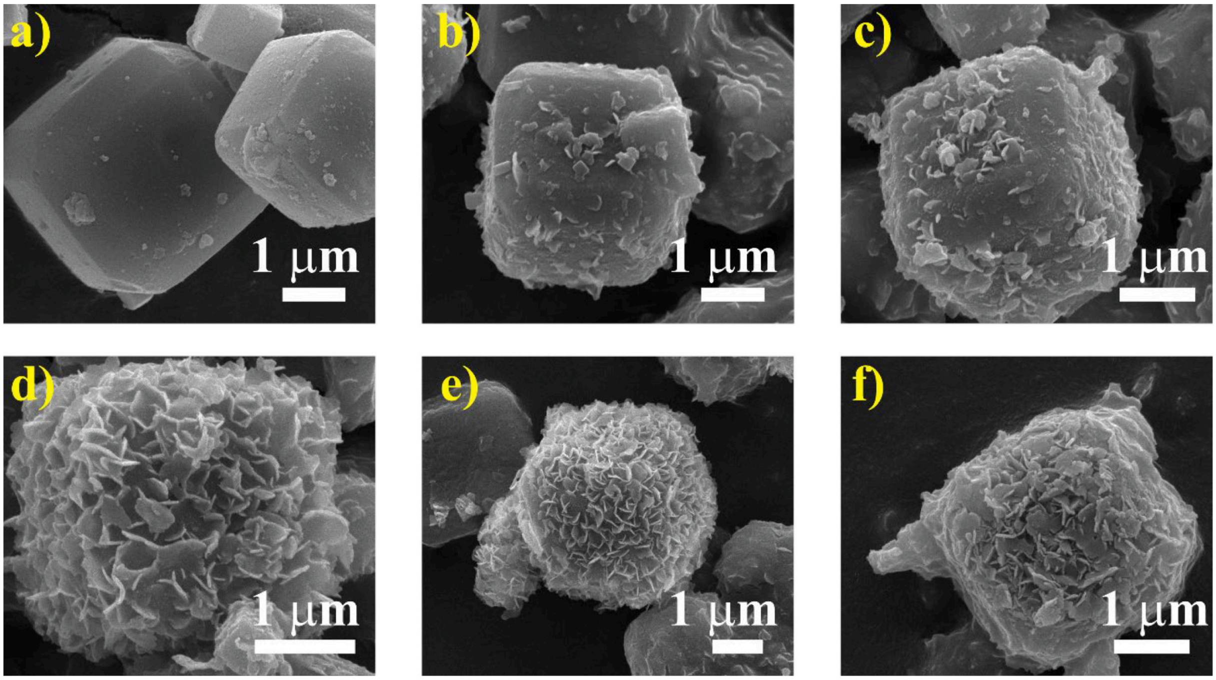

Fig. 1. SEM images of zeolite 4A (a) and LTA@Al-BDC syntheses at different Al/BDC molar ratios (b-f) correspond to Al/BDC ratios of 6, 5, 4, 3 and 2, respectively. All syntheses were carried out for 72 h.

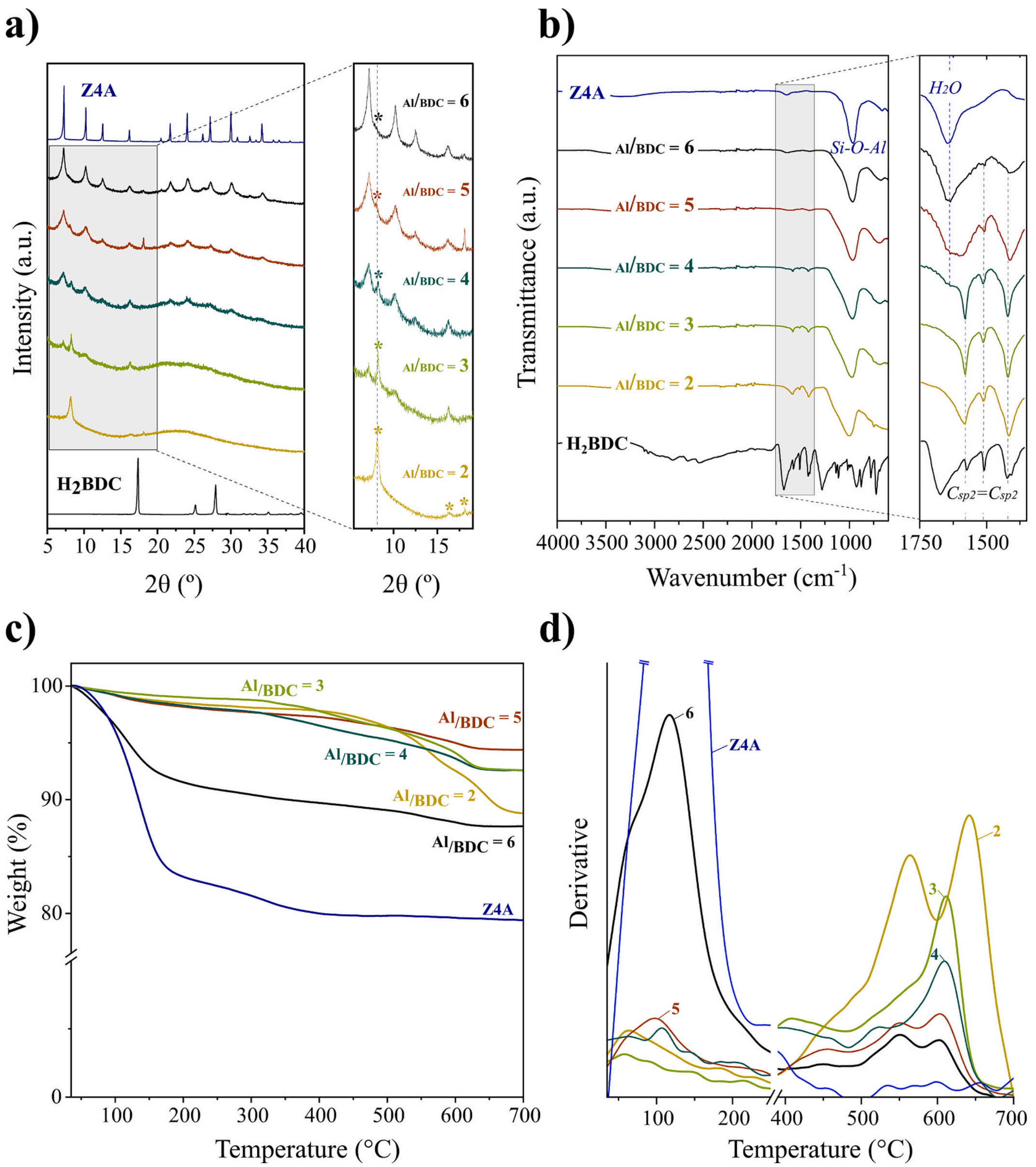

Fig. 2. Zeolite 4A (Z4A) and LTA@Al-BDC syntheses at different Al/BDC molar ratios: PXRD patterns (where the asterisk marks the peaks attributed to the Al-BDC MOF) (a), FTIR spectra (b), TGA (c) and DTG curves (d). All syntheses were carried out for 72 h.

disappears, probably due to the formation of a Lewis acid-base adduct. Asymmetric Si-O-Si and Si-O-Al stretching at 955 cm^{-1} are maintained from zeolite 4A in all hybrids, whereas the H_2O bending (1650 cm^{-1}) disappears as the material becomes less hydrophilic, which is attributed to the lack of weight loss at low temperature (due to the retained water molecules) as the Al/BDC ratio decreases reaching values of 2–5 (Fig. 2d).

Table 2 summarizes the yields corresponding to the MOF shell development, which have been estimated using the corresponding TGA curves and equation S1.

It can be noticed that using one half of the BDC equivalents (i.e. those needed for the total zeolite amorphization) almost doubles the yield when compared to using one third. Thereby, hereinafter an Al to BDC ratio of 2 was maintained. From the lattice parameters calculated for zeolite 4A, as the number of BDC equivalents increases, the lattice parameter for the inner zeolite increases until no zeolite phase is observed for Al/BDC = 2 (entry #1 from Table 2). The material that arises from the complete amorphization of the zeolite core can be conceived as an amorphous aluminosilicate core coated by a crystalline shell of MOF sheets. In other words, the X-ray diffraction of such material is solely caused by the crystalline shell and, as can be seen in Fig. S5, although there is a slight shift in the diffraction peaks when calcined, the structure does not suffer from the breathing phenomenon which is normally observed in MIL-53(Al) [30]. In this case, the zeolite particles serve as substrate and as aluminum source at the same time, thereby, the developed structure may have grown at fixed positions determined by the presence of aluminum atoms at the zeolite surface, which could explain the lack of structural flexibility.

3.1.2. *Time evolution*

With the aim of producing a genuine zeolite-MOF hybrid material that conserves the zeolite structure, the synthesis was constricted to shorter times. Monitoring the synthesis evolution by SEM observation, nucleation trigger points start forming during the first hour because non-zeolite spots seem to be discernible on the zeolite surface (Fig. 3a-c), which eventually develop into crystalline sheets after 8 h (Fig. 3d-f).

The so-called induction period is the time that takes from the reaction start to the development of crystalline phases [31]. As it is defined,

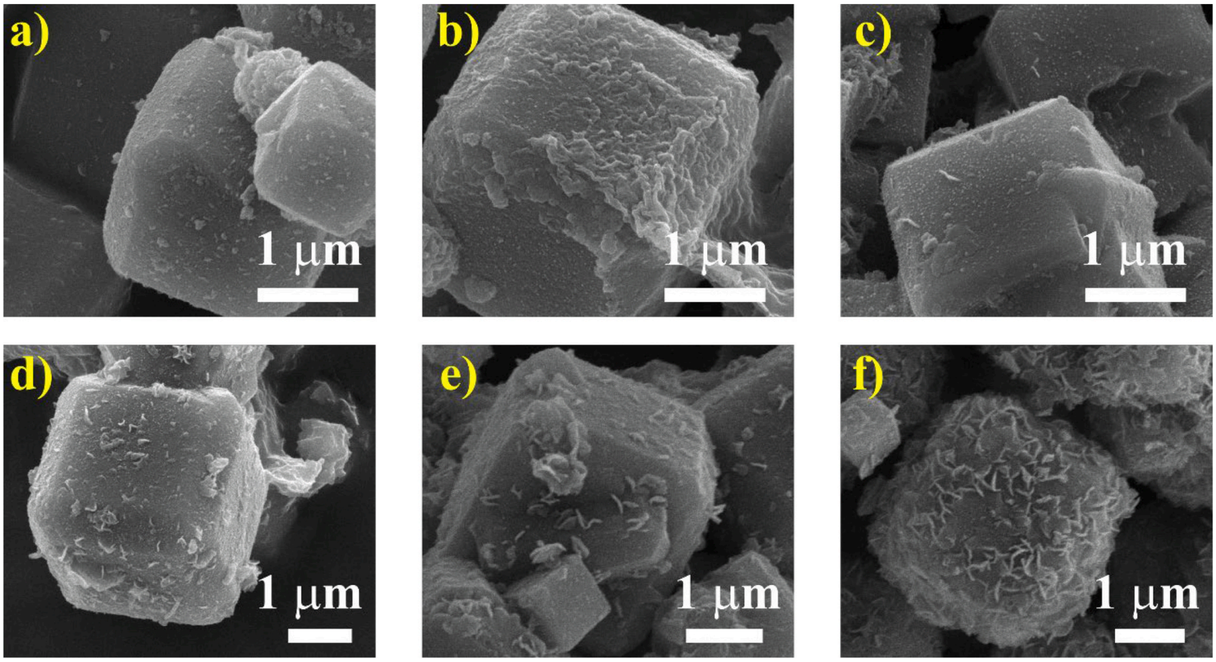

Fig. 3. SEM images of LTA@Al-BDC syntheses at Al/BDC molar ratio of 2 and different synthesis times: (a-f) correspond to 1 h, 2 h, 8 h, 12 h, 24 h and 48 h, respectively.

it depends on the characterization technique itself. Regarding TGA, the formation of the MOF-like shell implies an observable weight loss at around 400–700 °C (Fig. 4a), and it can be noticed in **Fig. S6** that after 8 h such loss substantially increases. These findings agree with the PXRD results, since the diffraction peak at ca. 2θ 8.1° starts to be appreciated also after 8 h (Fig. 4b). Although some non-zeolite material growth was evidenced after 1 h of reaction, as the SEM images shown (Fig. 3a), the detection of MOF PXRD peaks could have been hindered by the scarce amount of MOF formed during the first hours of reaction in comparison with the significant amount of zeolite 4A present. Hence, under these conditions, the shell formation could be considered as an initial nucleation step (<8h), in which crystallinity is not resolved by PXRD, followed by an induction period in which the MOF sheets start to appear (ca. 8 h) and, finally, a stage of crystal growth (>12 h). However, it is observed that as the synthesis time increases, the zeolite becomes more amorphous. Moreover, exposing the zeolite to H_2BDC only for 1 h was enough to appreciate some loss of crystallinity, as compared to the raw zeolite material (Fig. 4b), which will render a poor microporosity. This can be related to an initial proton exchange process (that would amorphize the zeolite) [28] running parallel to the aluminum leaching but quickly partially blocked by the growth of the MOF shell, otherwise the whole zeolite would become amorphous.

3.1.3. Influence of pH

As it has already been probed, acid conditions allow the BDC based structure to crystallize but at the same time convert the zeolite into an amorphous aluminosilicate, so there must be a compromise between the extraction of some aluminum atoms, and further collapse of the crystalline zeolitic structure, and MOF shell formation. Adjusting the amount of H_2BDC results in a variation of the pH at which the zeolite is

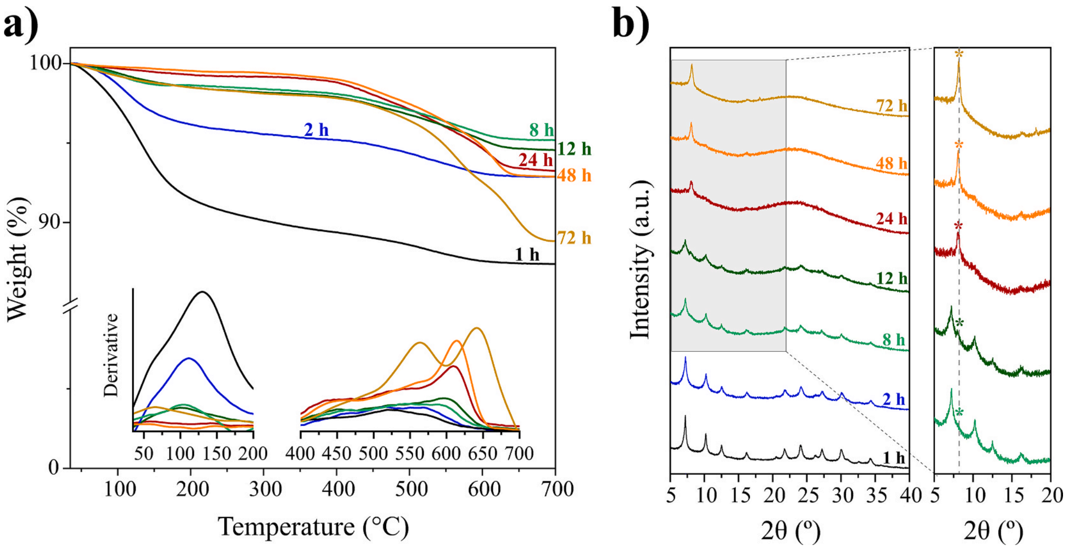

Fig. 4. LTA@Al-BDC syntheses at Al to BDC molar ratio of 2 and different synthesis times: TGA and DTG curves (a) and PXRD patterns (b), where the asterisk marks the peak at 2θ 8.1° corresponding to the Al-BDC MOF.

exposed (Table 2). The initial pH of the zeolite in water is around 11 in all cases, after the addition of H_2BDC in different proportions, pH ranged from 5.6 to 6.7. Alternatively, an initial H_2BDC solution was prepared adjusting its pH in the 3.9–9.7 range with NaOH. In this case, after the addition of the zeolite, the synthesis mixture pH ranged from 5.6 to 7.1. This latter approach seeks not only to reduce the acidic conditions, but also to increase the H_2BDC solubility and favor the deprotonation steps required during MOF formation. Moreover, it has already been reported that is possible to synthesize MIL-53(Al) in water at room temperature employing sodium terephthalate (Na_2BDC), the homologous organic salt of H_2BDC [32].

Starting with the H_2BDC solution at pH 5.1 seemed to have no distinct effect respect the pH 3.9, as the PXRD from Fig. 5a indicates. The synthesis resulted in the formation of a MOF-like shell coating an amorphous material (Fig. 6a and e).

At slightly softer conditions (pH 5.7), the material preserves the inner zeolite crystallinity (see PXRD of Fig. 5a) and features the characteristic loss of water (see TGA of Fig. 6e) even though the zeolite particles were greatly coated with MOF sheets (Fig. 6b). The shell formation yield of such synthesis was above 8 % (entry #13 from Table 2).

At pH 6.3 (Fig. 6c), H_2BDC was totally dissolved but, although the resulting material featured a similar FTIR spectrum and PXRD pattern than the former LTA@Al-BDC core shell material (Fig. 5b), neither the hydrophilicity nor the shell formation yield were enhanced (Fig. 6e).

Above pH 6.3, the H_2BDC solution behaves as a buffer until pH boosted to ca. 9, at which no MOF-like structures were formed (Fig. 6d). Under these conditions, the H_2BDC would appear fully deprotonated and the zeolite 4A is not degraded. Such milder conditions do not leach enough aluminum from the zeolite, neither to allow the amorphization of the zeolite nor to form the Al-MOF.

Based on these results, adjusting the pH to which the zeolite is exposed around 5.7 renders a trade-off in terms of covering the zeolite particles without destroying their characteristic crystallinity and microporosity as will be shown later. Moreover, that pH value sets the limit at which FTIR shows the H_2O bending band (1650 cm^{-1}) also observed for raw zeolite (Fig. 5b), while TGA exhibits the second water loss step due to the presence of tightly bonded H_2O molecules within the hydrophilic zeolite framework (Fig. 6e and **Fig. S7**a). Both evidences are related to the preservation of the zeolite structure.

3.1.4. *Influence of calcination*

It has been probed that zeolite calcination promotes the Si-O-Al bond cleavage occurring dealumination to some extent. Upon calcination, tetrahedrally coordinated aluminum atoms within the zeolite structure are released resulting in the formation of extraframework aluminum (EFAL) [33–35]. The crystallization of the BDC-based MOF shell starts at the surface of the zeolite particles and requires the extraction of some aluminum atoms. Therefore, a way to modify the zeolite surface towards a more reactive material could arise from calcining the raw powder and generating EFAL. In consequence, after calcination at 500 °C, the zeolite diffraction peaks widened and showed a slight shift (**Fig. S8**); however, the crystallinity remained almost unchanged. Calcined zeolite was employed as the raw material under the same conditions at which zeolite 4A microstructure was not preserved, as the Al/BDC molar ratio was 2 with the synthesis time ranging from 24 to 72 h. Interestingly, in this case, the resulting LTA@Al-BDC material did not lose entirely the zeolite core crystalline structure, as the PXRD pattern and its hydrophilic behavior (Fig. 7) indicate. Moreover, at 72 h, the shell formation yield was around 15 % (entry #16 from Table 2), which was the highest obtained. These results evidence that after calcination, the zeolite is more prompt to react towards shell crystallization, possibly due to the presence of EFAL. Besides, calcination could have modified the zeolite framework, generating defects or changing its surface chemistry, which could have boosted the MOF shell crystallization at an early stage, thereby protecting the zeolite from further H_2BDC attack.

As reaction time decreased, the weight loss due to the formation of shell sheets decreased as well, whereas the hydrophilicity (Fig. 7a) and zeolite crystallinity (Fig. 7b) remained similar, indicating that no further amorphization was produced from 24 to 72 h. Thus, it can be concluded that the calcination pretreatment of the zeolite favors the formation of a high amount of MOF sheets while preserving the structure of the zeolite. Therefore, there are two possible effective strategies to coat the zeolite with MOF without degrading its structure: pH control and calcination.

3.2. *Characterization of the LTA@Al-BDC structure*

In order to set a reliable comparison between zeolite 4A and the produced LTA@Al-BDC, it has been selected a hybrid that clearly preserves the zeolite structure and at the same time displays the features related to the Al-BDC MOF. This is the case for the LTA@Al-BDC entry #13 from Table 2. Moreover, as will be shown later, such hybrid is noteworthy in terms of adsorption.

Regarding the LTA@Al-BDC structure, PXRD probes its long-range order from which is assessed that a crystalline phase is growing onto

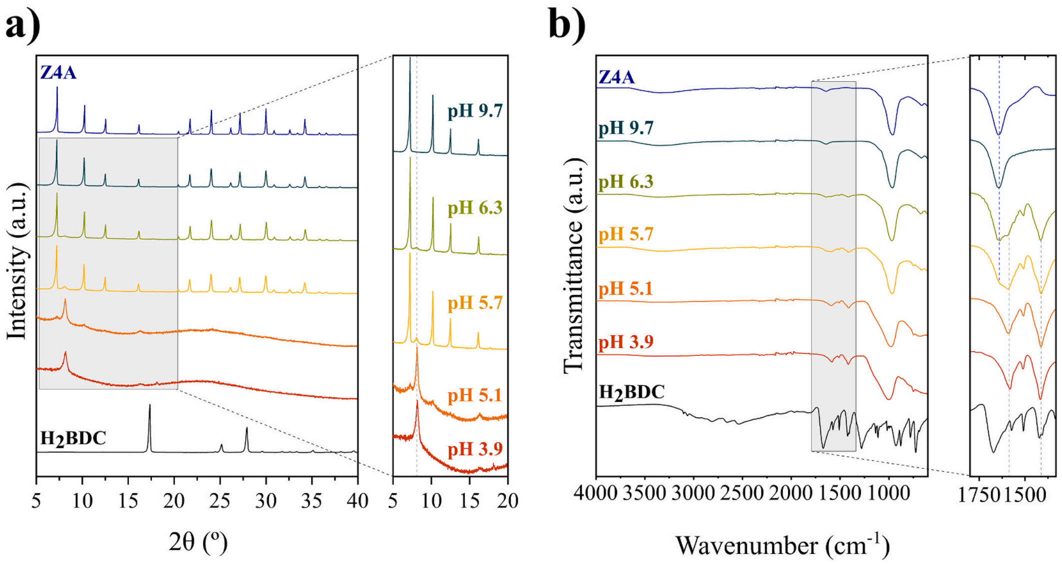

Fig. 5. PXRD patterns of zeolite 4A, H_2BDC and LTA@Al-BDC synthesis at different starting pH (a) and the corresponding FTIR spectra (b). All syntheses were carried out for 72 h and Al to BDC molar ratio of 2.

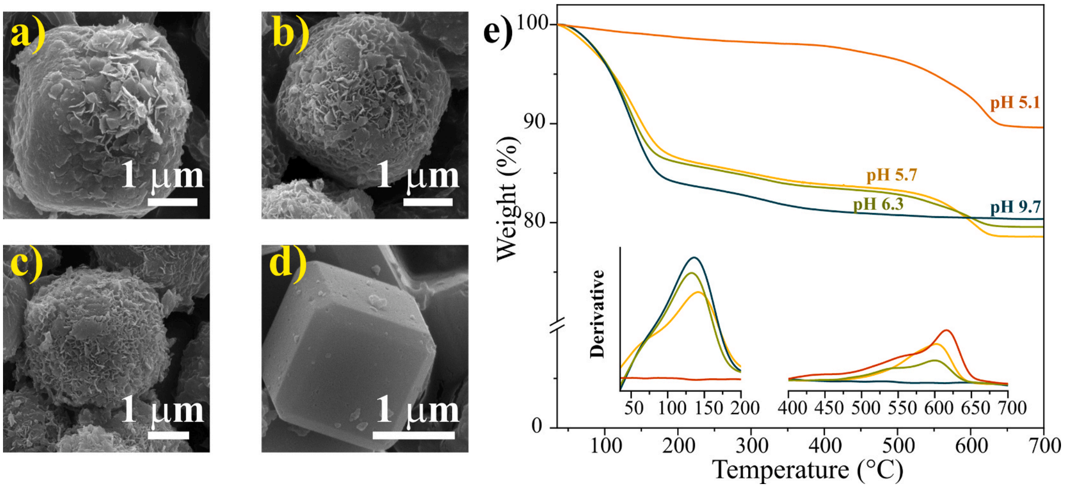

Fig. 6. SEM images of LTA@Al-BDC syntheses at different starting pH values (a-d correspond to pH 5.1, 5.7, 6.3 and 9.7 respectively), TGA and DTG curves (e). All syntheses were carried out for 72 h.

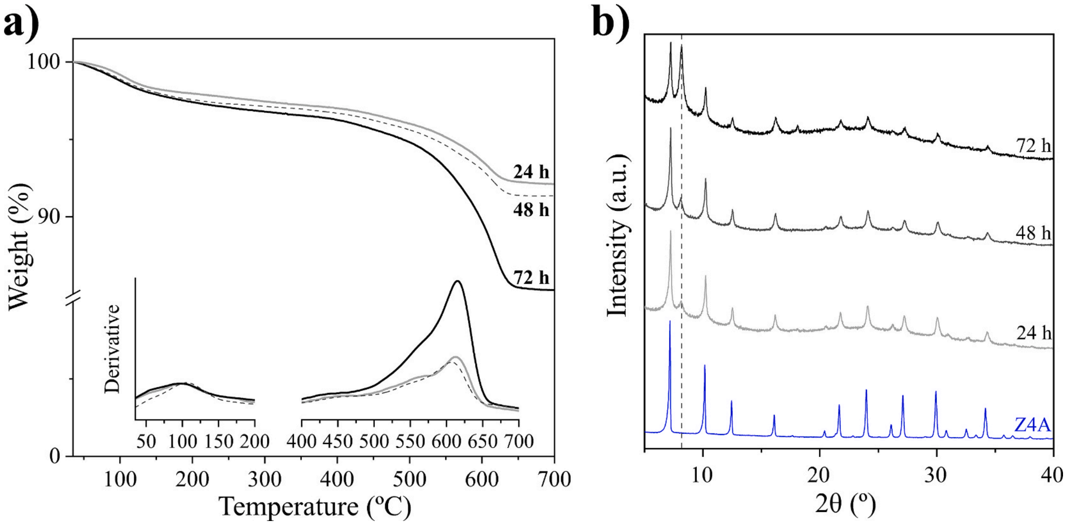

Fig. 7. LTA@Al-BDC syntheses at Al/BDC molar ratio of 2 and different synthesis times (24–72 h) employing calcined zeolite (500 °C 4 h): TGA and DTG curves (a) and PXRD patterns (b).

the zeolite particles. To further characterize how the zeolite is converted into a core–shell zeolite@MOF, it is necessary a tool to probe its local structure. For that, ^{29}Si and ^{27}Al solid-state NMR are sensitive to the local environment of silicon and aluminum, respectively.

Generally, ^{29}Si MAS NMR spectra of zeolites show different peaks arising from tetrahedrally coordinated silicon (Q^4), whose shift depends on the distribution of silicon and aluminum atoms bonded to the central silicon atom $Si(OSi)_{4-x}(OAl)_x$. There are five possible distributions, corresponding to $x = 0, 1, 2, 3$ and 4, given rise to five different resonances [4,36]. ^{29}Si MAS NMR spectra of zeolite 4A displays a single signal at −90.1 ppm (Fig. 8a) caused solely by $Si(OAl)_4$ units [37]. Furthermore, the absence of the other potentially possible Q^4 resonances probes a Si to Al ratio of 1 for the raw zeolite 4A. Conversely, in the LTA@Al-BDC ^{29}Si MAS NMR spectrum, although keeps the signal at −90.1 ppm, broad shoulders appear at ca. −86.2, −96.1 and −105.5 ppm (Fig. 8c) attributed to $Si(OH)(OAl)_3$ (Q^3), $Si(OSi)_1(OAl)_3$ (Q^4) and $Si(OSi)_2(OAl)_2$ (Q^4) units respectively. These new Q^4 signals are consistent with a weak dealumination [38], while the Q^3 points to a partial amorphization, both caused by exposing the zeolite to an acidic medium.

Moreover, given that the Loewenstein's rule prohibits the presence of Al-O-Al bonds in zeolites [39], there is only a possible coordination environment for framework aluminum: $Al(OSi)_4$, which simplifies the ^{27}Al MAS NMR spectra of zeolites. Nevertheless, ^{27}Al MAS NMR spectra can show different shifts for tetrahedral (framework aluminum), pentahedral and octahedral coordinations. Hence, it can be used to identify the presence of Al in a different coordination as a result of MOF crystallization. The ^{27}Al MAS NMR spectrum of zeolite 4A consists of a main signal at ca. 60.1 ppm ascribed to tetrahedral Al [38], and a weak peak at ca. 2.7 ppm possibly due to the presence of residual *hexa*-coordinated EFAL (Fig. 8b). The latter signal is slightly shifted and clearly enhanced in the LTA@Al-BDC ^{27}Al MAS NMR spectrum (Fig. 8d). This indicates an increase in *hexa*-coordinated aluminum due to the formation of the aluminum-based MOF. Similarly to MIL-53(Al) [30], the resulting MOF shell is based on octahedrally coordinated aluminum atoms with BDC ligands.

TEM can provide more detailed morphological, structural and chemical information of the LTA@Al-BDC, to further complete its characterization. The obtained images allow to determine the intimate contact between the zeolite and the MOF (Fig. 9).

Bright-field images, in which the contrast is given by the different density of the two crystalline materials, allowed to measure the shell

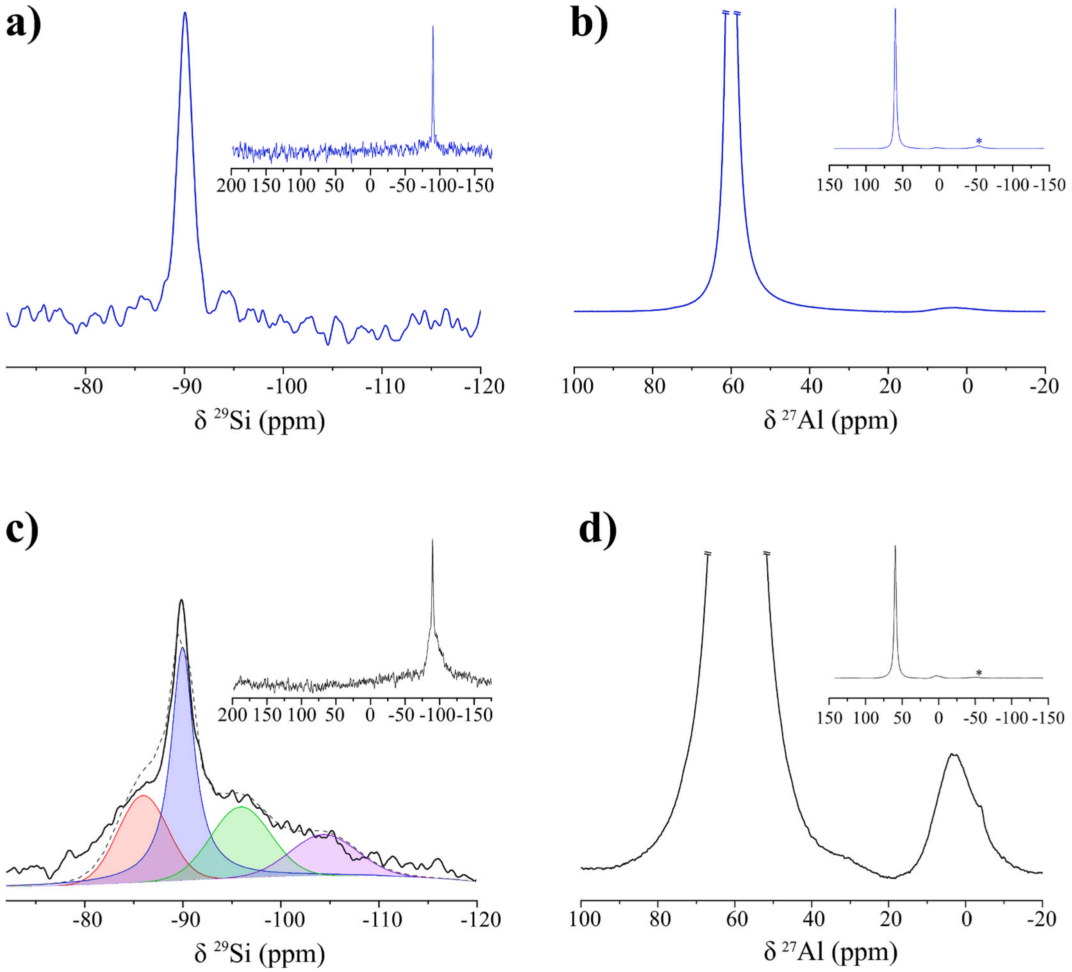

Fig. 8. ^{29}Si CP-MAS and ^{27}Al HPDec-MAS NMR spectra (left and right respectively) of zeolite 4A (a and b) and LTA@Al-BDC synthesis of entry #13 from Table 2 (c and d). Asterisks indicate spinning sidebands.

thickness, ca. 182 nm, owing to the lower density of the thin MOF sheets in comparison with the zeolite core (Fig. 9a). Moreover, it was possible to identify the two different phases separately and altogether by selective area electron diffraction (SAED). Fig. 9d was acquired from an ultrathin specimen of LTA@Al-BDC, the observed SAED pattern is characteristic for the cubic system of the LTA-type zeolite probing that the zeolite core crystalline structure was retained after the synthesis; bright spots at d-spacings 12.9 and 9.2 Å were correlated with zeolite planes (200) and (220), respectively. To observe the diffraction that arises from crystalline shell sheets, it was necessary to disperse directly the as-synthesized LTA@Al-BDC in powder state. SAED pattern of shell sheets (Fig. 9e) took multiple MOF crystals with different orientations; therefore, it shows two diffraction halo-rings, instead of well-defined spots, whose d-spacings are ca. 11.6 and 5.9 Å, similar to those obtained from PXRD for the proposed planes (011) and (022) of the MOF (**Table S1**). Interestingly, the TEM image from **Fig. S9** probes the crystallinity of the shell sheets as it was possible to observe a periodic pattern related to ordered atomic arrangements. Fig. 9b exhibits a well-defined LTA@Al-BDC particle in whose SAED both phases are featured, bright spots related to the zeolite planes and the two halo-rings (associated d-spacings of 11.6 and 5.9 Å) that correspond to the MOF. In some cases, it can be distinguished a gradient contrast at the zeolite interface suggesting that the MOF growth is surrogated to the aluminum leaching and partial zeolite amorphization (**Fig. S10**).

In dark-field images (Fig. 9c), the contrast depends on the different atomic number of the atoms that constitute the two hybridizing materials. Chemical analysis was performed across the line profile shown in Fig. 9c. Si and Al counts are displayed including the quantified Si/Al ratio (Fig. 9f). As expected, within the bulk of the LTA@Al-BDC particle total counts increase, being maximum in the region in which a smaller particle (brightest part) is superimposed onto the bigger one; the Si/Al ratio in that zone is around 1. For the MOF shell, even though the total counts decreased, the aluminum counts remain remarkable probing that the crystallized MOF is based on Al. To confirm these results, it was performed an EDX chemical composition mapping from an ultrathin section of the LTA@Al-BDC specimen, employing a probe aberration-corrected TEM microscope in STEM mode which has a superior resolution. The compositional mapping clearly shows that the shell is composed of aluminum (Fig. 9g-j) rather than silicon. Such feature can be as well intuited in the EPMA elemental mapping from **Fig. S11**, reaffirming both analysis the formation of the Al-BDC.

3.3. Gas adsorption

CO_2 adsorption properties of zeolite 4A have been greatly reported [40]. Its pore size being around 0.4 nm, it is grouped as a small-pore zeolite. Thus, its CO_2 adsorption behavior is not only defined by electrostatic interactions but also by size exclusion and surface diffusion [41]. Although CO_2 molecules are nonpolar, they have a large quadrupole moment and higher polarizability than other molecules such as N_2, which is also nonpolar (Table 3).

Zeolite 4A affinity towards CO_2 occurs through zeolite surface electrostatic interactions, which depends on its Al content, and owing to the lower kinetic diameter of CO_2 when compared to N_2. Therefore, zeolite

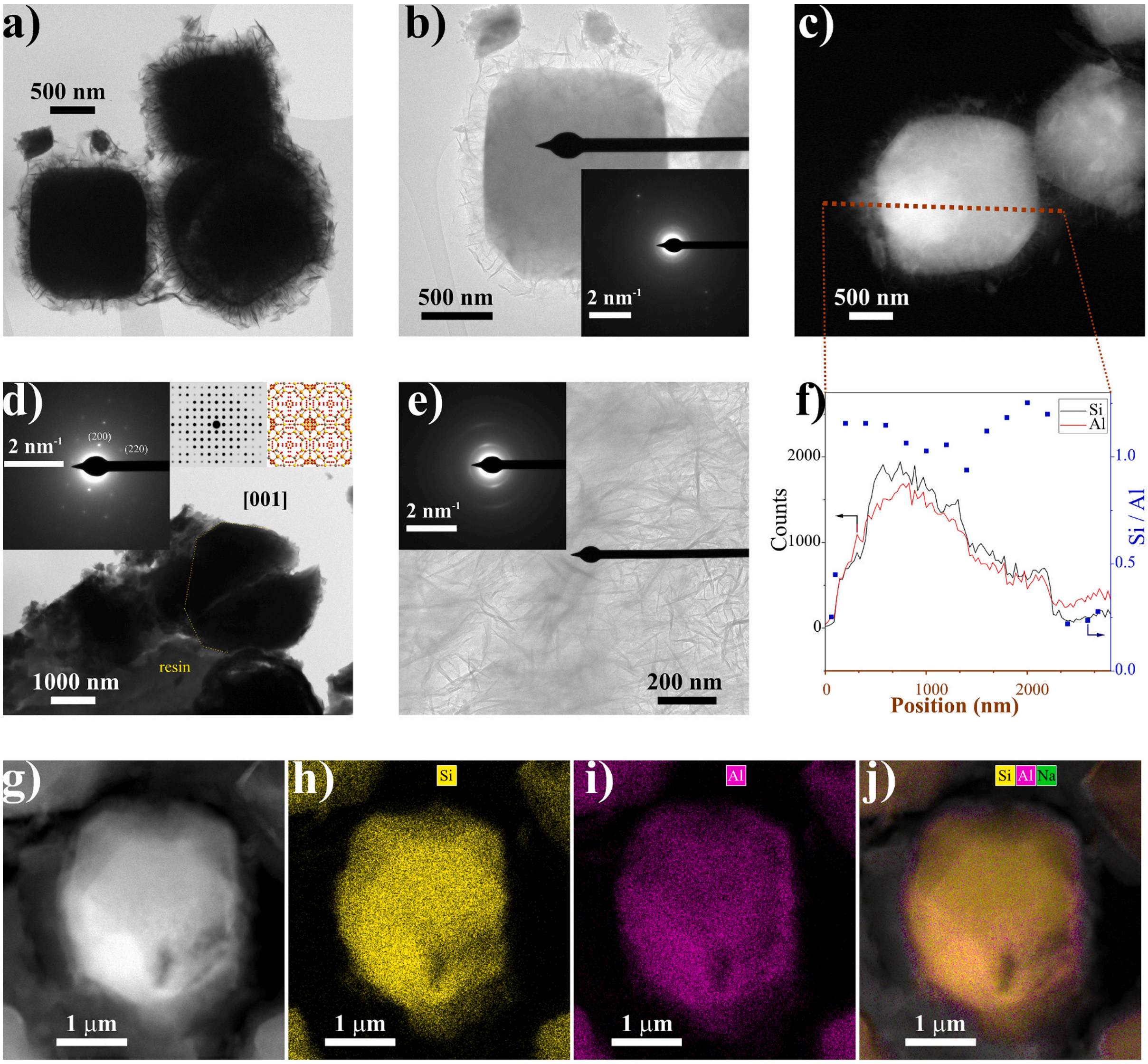

Fig. 9. TEM images of LTA@Al-BDC (entry #13 synthesis from Table 2). Bright-field images (a, b, d and e) in which their respective SAED patterns appear superimposed (b, d and e). Image d) shows, for an ultrathin specimen, the indexation of the simulated single crystal diffractogram and model for LTA-type zeolite along the [001] zone axis. Dark-field image acquired in STEM mode (c) accompanied with the line profile scan of Si and Al atoms, and the corresponding quantified Si to Al ratio (f). STEM chemical mappings of an ultrathin specimen of the LTA@Al-BDC (g-j). Dark-field image (g). EDX imaging: Si (h), Al (i) and mixed compositional, including Si, Al and Na (j).

Table 3
Relevant properties of CO_2, N_2 and H_2 gases [4,41].

Probe	**Kinetic diameter** (nm)	**Polarizability** x10^{-30} (m^3)	**Quad. moment** x10^{-24} (esu cm^2)	**Dipole moment** (esu cm)
CO_2	0.330	2.65	4.30	0
N_2	0.364	1.76	1.52	0
H_2	0.289	0.80	0.66	0

4A is selective to CO_2 adsorption and shows negligible N_2 adsorption.

To set a comparison among the different materials produced and looking forward to relating its original microporosity with its adsorption features, CO_2 and N_2 adsorption were measured for the LTA@Al-BDC syntheses that lasted 72 h with an Al/BDC ratio of 2 but under other different conditions as indicated in Table 2: entry #1, entry #13 in which the pH is controlled and entry #16 in which zeolite is calcined. As stated, raw zeolite 4A shows high CO_2 adsorption capacity (up to 4.5 mmol·g^{-1} at 100 kPa and 0 °C) and insignificant N_2 uptake (Fig. 10). Importantly, the capacity of pore filling is determined by the accessibility to the probe molecules [42]. From the N_2 adsorption–desorption isotherm, it can be confirmed that the zeolite 4A microporosity is not accessible to N_2. Owing to its higher kinetic diameter, in the range of the pore openings, lower quadrupole and polarizability, the calculated specific surface area by the Brunauer-Emmett-Teller method (BET SSA), shown in Table 4, is almost negligible.

Contrarily, it has been demonstrated the usefulness of CO_2 adsorption at 0 °C and sub-atmospheric pressures for the characterization of small-pore zeolites [43]. According to the IUPAC, the obtained CO_2 adsorption isotherm is categorized as type I, which is given by microporous solids [44]. At low pressure, CO_2 uptake increases rapidly due to micropore volume filling. In consequence, micropore width was assessed by the Horvath-Kawazoe (HK) approach related to CO_2 adsorption. These results are shown in **Fig. S12**a, which exhibits a pore width around 0.5 nm, as expected for zeolite 4A. Micropore volume and equivalent SSA were evaluated by the Dubinin-Radushkevich (DR) method regarded to CO_2 physisorption as well, as it has been reported its suitability to characterize zeolite 4A [43]. The micropore volume is 0.33

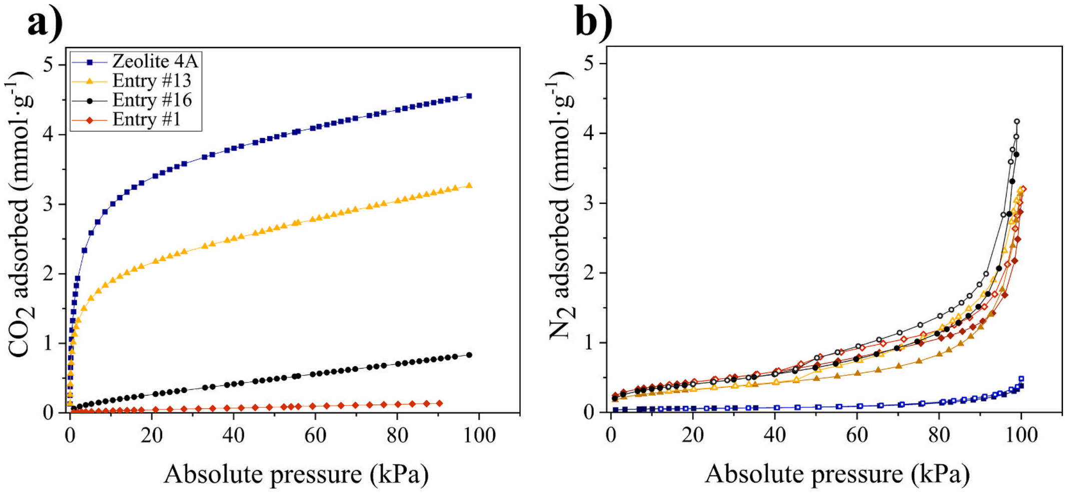

Fig. 10. CO_2 (a) and N_2 (b) adsorption isotherms at 0 °C and −196 °C respectively, for zeolite 4A (blue squares) and LTA@Al-BDC synthesis of entries #1 (orange diamonds), #13 (yellow triangles) and #16 (black circles) from Table 2. Opened symbols are used for desorption data.

Table 4
Textural properties of zeolite 4A, LTA@Al-BDC syntheses at Al to BDC molar ratio of 2 starting at pH values of 3.9 and 5.7, and employing calcined zeolite (entries #1, 13 and 16 from Table 2, respectively).

Sample	CO_2		N_2	
	V_{micro}[a] ($cm^3·g^{-1}$)	S_{DR}[a] ($m^2·g^{-1}$)	S_{BET}[b] ($m^2·g^{-1}$)	S_{BET}[b*] MOF ($m^2·g^{-1}$)
Zeolite 4A	0.33	812	5	–
Entry #1	–	22	36	228
Entry #13	0.14	352	27	267
Entry #16	–	75	33	187

[a] Limiting micropore volume (V_{micro}) and equivalent SSA (S_{DR}) applying the DR method to CO_2 adsorption isotherm at 0 °C.

[b] BET SSA (S_{BET}) calculated employing the N_2 adsorption isotherm at −196 °C in the range of p/p° 0.07–0.18, fulfilling the Rouquerol criteria [46].

[*] Related to the MOF shell by correcting the S_{BET} with the yields from Table 2.

$cm^3·g^{-1}$, which is similar to the micropore volume estimated by XRD for zeolite 4A (0.36 $cm^3·g^{-1}$) [43]; while the SSA is 812 $m^2·g^{-1}$ (Table 4). Both values are similar to those reported for commercial zeolite 4A through the DR method (0.32 $cm^3·g^{-1}$ and 684 $m^2·g^{-1}$) [45].

Conversely, CO_2 adsorption for LTA@Al-BDC synthesis starting at pH 3.9 (entry #1 from Table 2) was drastically reduced (Fig. 10a), resulting in a negligible micropore volume (Table 4). Such results are aligned with the loss of zeolite crystallinity already mentioned (Fig. 5a). Under these conditions, the zeolite microstructure tends to collapse, leading to a hydrophobic material whose adsorption properties are now related to a core–shell that comprises an amorphous aluminosilicate coated by MOF crystalline sheets. In this case, N_2 adsorption increases in the low-pressure region, possibly due to the MOF porosity and features a hysteresis loop above 50 kPa and a step increase in the high-pressure region (Fig. 10b), which can be attributed to N_2 capillary condensation in between the MOF sheets. The Barrett-Joyner-Halenda (BJH) method analyzes the pore size distribution (PSD) from N_2 adsorption, proving a PSD around 3.5 nm that did not appeared in raw zeolite 4A (**Fig. S12**b-c). The calculated BET SSA accounts for the MOF shell and considering the yield from Table 2, the crystallized MOF surface area would be around 228 $m^2·g(MOF)^{-1}$ (Table 4), such low SSA could be explained due to its nanosheet appearance.

For the synthesis in which the zeolite was previously calcined (entry #16 from Table 2), some zeolite crystallinity was preserved. Nevertheless, it was not sufficient in terms of CO_2 adsorption (<1 mmol·g^{-1} at 100 kPa and 0 °C, Fig. 10a). Moreover, HK PSD evidenced the loss of the original microporosity, as well as it happened with the LTA@Al-BDC from entry #1 (**Fig. S12**a).

It has been demonstrated that adjusting the pH conditions allows the MOF like shell to grow without compromising the core structure. In fact, in the synthesis at pH 5.7 (entry #13 from Table 2), the zeolite crystallinity was retained (Fig. 5a) as it happened with its adsorption properties. Although CO_2 adsorption decreased a bit (Fig. 10a), the isotherm featured the same type I shape given by microporous solids and an acceptable CO_2 uptake: 3.3 mmol·g^{-1} vs. 4.5 mmol·g^{-1} for pure zeolite both at 100 kPa and 0 °C. HK PSD (**Fig. S12**a) shows that the zeolite microstructure was not distorted, even though DR evidences some degree of amorphization (Table 4). Whereas the N_2 adsorption isotherm features a slight increase in the low-pressure region, a step increase in the high-pressure region and the hysteresis loop ascribed to inter-sheet condensation (Fig. 10b). From N_2 adsorption, the BJH method reveals the PSD around 3.5 nm (**Fig. S12**b-c) while the BET SSA related to the MOF shell is 267 $m^2·g(MOF)^{-1}$ (Table 4) of the same order as the one previously calculated.

To gain insight into the porosity of such materials, Fig. 11 contains the excess adsorption isotherms for H_2 at 25 °C up to 8000 kPa for the zeolite 4A and for the LTA@Al-BDC syntheses that stand out as the more representative examples: on the one hand, the synthesis in which pH was adjusted to 5.7 (entry #13 from Table 2) accounts for an LTA@Al-BDC in which the zeolite core is barely degraded; and on the other hand, the synthesis in which the zeolite was previously calcined (entry #16 from Table 2) represents the case in which zeolite is clearly amorphized.

The results show that while pure zeolite 4A demonstrates the highest H_2 adsorption, it is strongly decreased for the calcined zeolite derived material. Such small H_2 adsorption can be associated to the external surface detected in that material from the N_2 adsorption characterization (Table 4). Whereas the adsorption is only somewhat decreased compared to the zeolite 4A in the material prepared at pH 5.7, in which the zeolite structure is essentially maintained. Specifically, at the maximum measured pressure of ca. 8000 kPa, the adsorption of zeolite 4A is 0.834 mmol·g^{-1} while in the optimized LTA@Al-BDC sample is 0.747 mmol·g^{-1}.

These results suggest that the LTA@Al-BDC synthesis in which the pH is adjusted to 5.7 (entry #13 from Table 2) readily preserves the inner zeolite features, providing a synergistic effect of both materials: combining the zeolite microporosity, that renders a high CO_2 uptake, with the external properties of the MOF. This is of great importance when trying to form polymeric composites with the material.

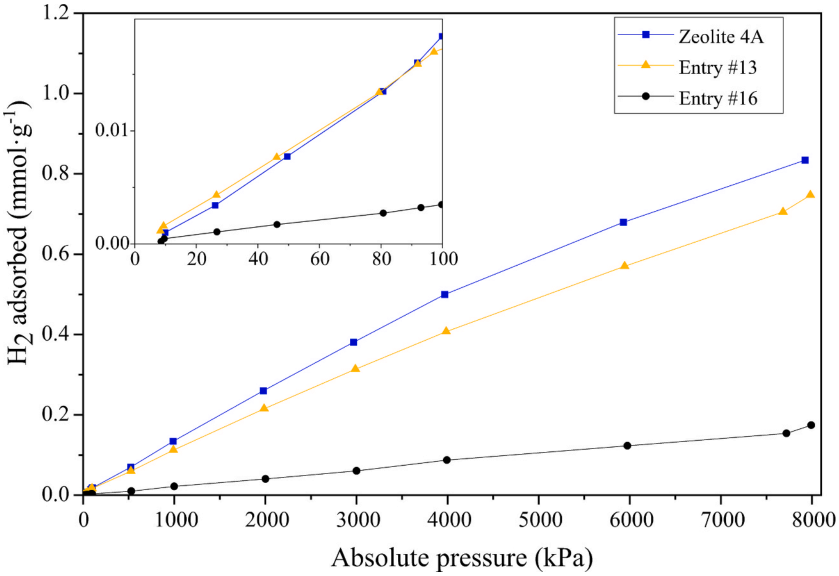

Fig. 11. Excess adsorption isotherms for hydrogen at 25 °C for zeolite 4A (blue squares) and LTA@Al-BDC synthesis of entries #13 (yellow triangles) and #16 (black circles).

3.4. *Evaluation of the CO_2 adsorption*

To improve the scope of the CO_2 adsorption performance, it has been evaluated its adsorption at 25 °C on LTA@Al-BDC (entry #13) and the bare zeolite 4A (Fig. 12).

As expected, in both cases CO_2 adsorption decreases as temperature increases. All isotherms exhibit the IUPAC type I shape, probing micropore filling. Compared to the MOFs ZIF-8, ZIF-94, MIL-53(Al) and NH_2-MIL-53(Al), which have been reported as CO_2 adsorbents, the LTA@Al-BDC exhibits a higher CO_2 adsorption at 0 °C and 25 °C in the low-pressure range, given its microporosity (**Table S2**). This feature can also be observed in comparison with some reported porous carbons applied for carbon capture, utilization and storage [47–49], suggesting that the LTA@Al-BDC outperforms other adsorbents in applications where CO_2 concentration is low, such as direct air capture [50].

Moreover, considering such low-pressure range in which micropore adsorption and diffusion occur, the time-dependent CO_2 adsorption for zeolite 4A and LTA@Al-BDC (Fig. 13) follows the pseudo-second order model presented by Ho and McKay (Equation S5) [51]. According to this model, the CO_2-adsorbent interaction is expected to be caused by the strong interaction between CO_2 and the surface of the adsorbent, which determines the overall adsorption rate [52]. Although CO_2 adsorption is reduced to some extent in the LTA@Al-BDC, it presents similar constant rates of adsorption than zeolite 4A (**Table S3**), especially in the lowest pressure point, in which only micropore filling occurs. Fig. 13 shows that the pseudo-second order isotherm model fits better at lower equilibrium pressure points. At higher pressures, differences in external surface adsorption may result in slight deviations from the proposed model. Therefore, it can be concluded that CO_2 adsorption occurs similarly than in the raw zeolite and is ruled by strong CO_2-zeolite interactions.

3.5. *IAST selectivity*

Apart from the high adsorption capacity, adsorbents have to be selective towards a specific adsorbate and discriminate others. To further assess the adsorption behavior of the LTA@Al-BDC from entry #13, it was considered its applicability regarding CO_2/N_2 separation. Seeking that purpose, the Ideal Adsorbed Solution Theory (IAST), introduced by Myers and Prausnitz in 1965 [53], allows to predict mixed gas adsorption experiments using pure-component adsorption isotherms. Such theory can be applied to characterize adsorbents towards different separations as for instance, CO_2/N_2 [54]. For IAST calculations, pure

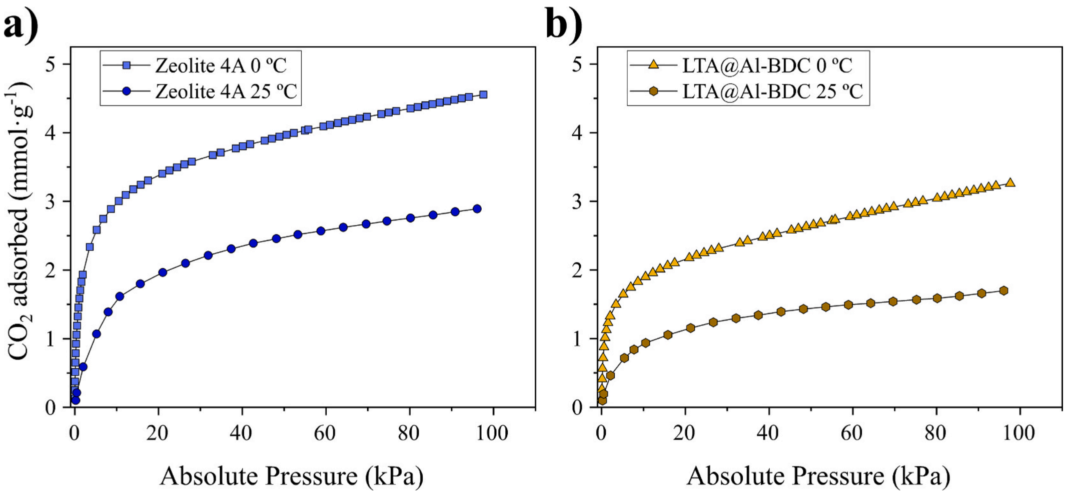

Fig. 12. CO_2 adsorption isotherms at 0 °C and 25 °C for zeolite 4A (a) and LTA@Al-BDC of entry #13 from Table 2 (b).

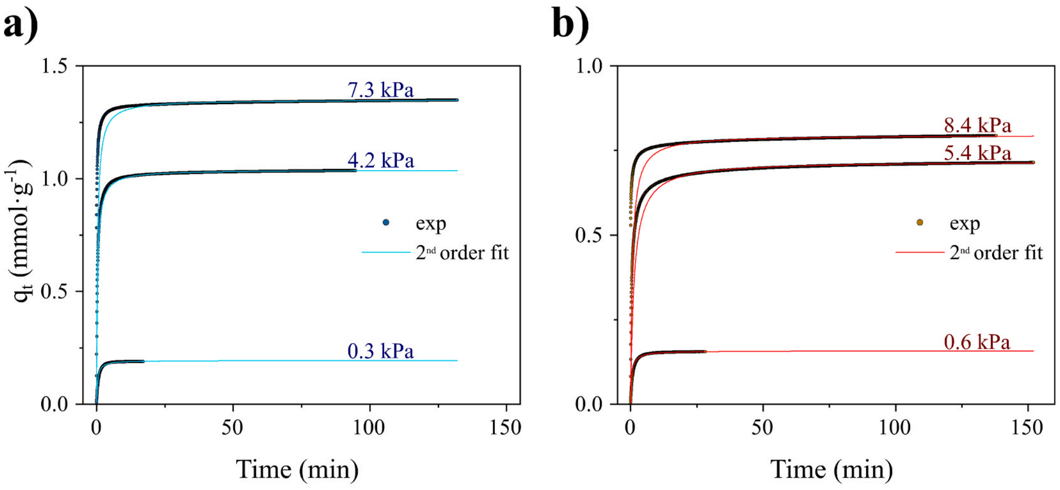

Fig. 13. Experimental CO_2 uptake at 25 °C on zeolite 4A (a) and on LTA@Al-BDC of entry #13 from Table 2 (b) alongside with the predicted uptake by the pseudo-second order model.

component isotherms have to be collected roughly at the same temperature, so N_2 adsorption was registered at 0 °C as well.

Fig. 14a shows the recorded adsorption isotherms for CO_2 and N_2 at 0 °C alongside with their fittings. At that temperature, N_2 is above its critical point, hence is non-condensable and, in consequence, does not feature the hysteresis loop in the high-pressure region as previously observed. Moreover, its adsorption is clearly reduced and is directly proportional to the partial pressure of the adsorbate following Henry's law. Regarding Henry's fit, caution must be taken, as unrealistically adsorption increases constantly with pressure, so the IAST calculation was not extrapolated to pressures higher than 300 kPa. In the case of CO_2, the best fit was given by the Redlich Peterson (RP) model [55], a three-empirical parameter model (Equation S11). In any event, once pure component isotherms were fitted, the IAST model allowed to predict CO_2-N_2 mixture composition isotherms at different total pressures, from which the CO_2/N_2 selectivity was calculated at a 15:85 M composition, which is typically found in post-combustion streams, as a function of total pressure (Fig. 14b).

At low pressures, in agreement with the pure component isotherms, the LTA@Al-BDC greatly adsorbs CO_2 over N_2 resulting in a predicted IAST selectivity above 1000 at 25 kPa. As the system pressure increases, the IAST selectivity lowers but, in any case, the material preferentially adsorbs CO_2 over N_2. At 100 kPa, the LTA@Al-BDC shows an IAST selectivity of ca. 350. Compared with reported IAST selectivity predictions for other CO_2 adsorbent materials (**Table S4**), LTA@Al-BDC proves to be promising.

3.6. *Water uptake and preliminary polymer composite*

Moreover, apart from the high CO_2/N_2 IAST selectivity, the hybrid material benefits from having a more hydrophobic shell and an improved interaction with polymers. **Fig. S14** shows the water uptake of the hybrid material and the former zeolite. While the zeolite 4A water uptake at 24 h is 22 wt%, such value is reduced to 5 wt% for the LTA@Al-BDC (entry #13 from Table 2) and only increases to 7 wt% after 48 h (this being 24 wt% for the zeolite). Owing to its high content of extra-framework cations, zeolite 4A tends to adsorb not only CO_2 but also H_2O through electrostatic interactions, showing a greater affinity for the latter due to its high dipole moment [56]. The presence of moisture is a major concern regarding gas separation at industrial scale, since using completely dry feed-gas streams increases costs and may render the entire process economically unfeasible. Therefore, the higher hydrophobicity of the hybrid material demonstrates its superiority over other adsorbents, as some authors did with their zeolite@MOF hybrid

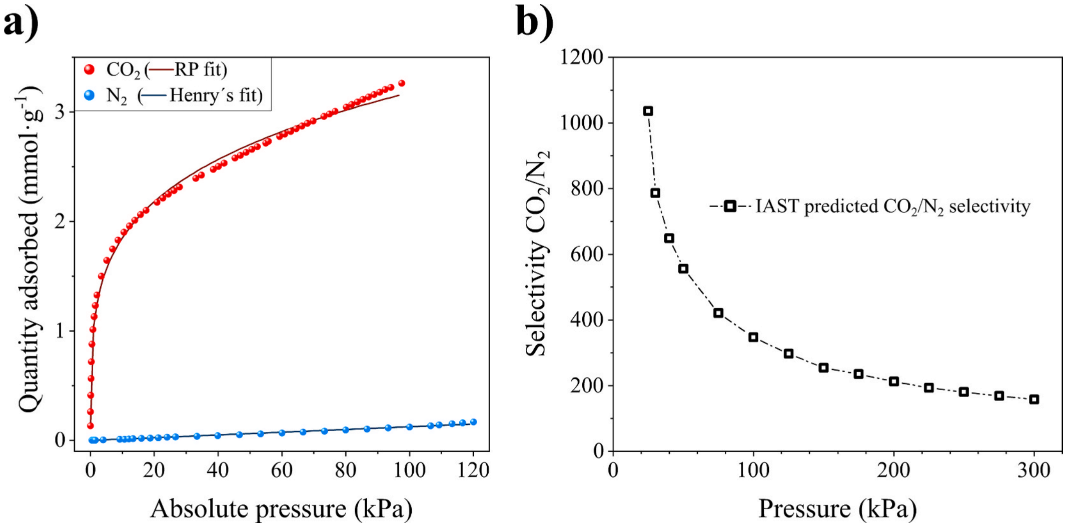

Fig. 14. LTA@Al-BDC (entry #13 from Table 2) adsorption isotherms at 0 °C for CO_2 (red) and N_2 (blue) alongside with their proposed fittings (a); and IAST predicted CO_2/N_2 selectivity for 15:85 composition at 0 °C as a function of the total pressure (b).

materials attending to the more hydrophobic nature of the shell [12,13].

Finally, the suitability of the hybrid material as filler for mixed matrix membranes was preliminary established formulating a 5 wt% polymeric composite with Pebax® Rnew®, a membrane polymer that has demonstrated a remarkable CO_2 separation performance in combination with MOF type fillers [57]. As **Fig. S15** depicts, the bare zeolite shows evident aggregation and the non-desirable “sieve-in-a-cage” morphology [58], while the hybrid filler, due to the coating of the zeolite 4A particles with MOF-like material, seems to be perfectly interacting and embedded with the surrounding polymer. This follows some results presented in the literature, in which the MOF shell enhances the compatibility between the polymer and the zeolite@MOF [14]. In fact, the enhanced filler-polymer interaction arises from the nanosheet-like morphology of the LTA@Al-BDC surface and the higher hydrophobicity of the crystalline shell. The former is probed by the increase in the S_{BET} (Table 4) while we have demonstrated the latter by monitoring the water uptake.

4. Conclusions

The formation of a core–shell porous material comprising a zeolite 4A core and an Al-BDC based MOF shell has been achieved. It has been evidenced that the synthesis is based on the chemical attack of the zeolite 4A with H_2BDC, resulting in the leaching of the aluminum from the zeolitic framework, thus making possible the subsequent MOF crystallization as sheet-like particles around the zeolite crystals. MOF growth causes partial degradation of the zeolite, the use of two different strategies as they are the calcination of the raw zeolite before the synthesis and controlling the pH, allowed to retain the zeolite structure coexisting with the MOF.

A detailed characterization of the adsorption properties of the synthesized materials has been carried out. It has been seen that CO_2 and H_2 adsorption are directly related to zeolite microporosity, which in turn indicates a trade-off in terms of MOF growth and zeolite amorphization. At certain synthesis conditions (mild initial pH values or precalcination of the zeolite) a synergistic effect of both materials can be achieved: combining the preserved zeolite microporosity, which renders a high CO_2 uptake, with the external surface area properties of the MOF. Under the optimal synthesis conditions of the LTA@Al-BDC (72 h, Al/BDC molar ratio 2 and $pH = 5.7$ of BDC solution), the characterization techniques used (TGA, electron microscopies, XRD and NMR) show a core that maintains the zeolite structure surrounded by a crystalline MOF shell of ca. 182 nm. The MOF shell grows as high aspect nanosheets based on octahedrally coordinated aluminum atoms with BDC, forming a rigid structure. It is also suggested that in the connection of both materials, the zeolite and the MOF may share some aluminum atoms, thus contributing to the generation of a hybrid structure at the atomic scale. Both CO_2 and H_2 adsorption measurements suggest that the LTA@Al-BDC sample obtained under optimum synthesis conditions preserves the inner zeolite features. In fact, the CO_2 adsorption of LTA@Al-BDC follows the same pseudo-second order model as that of zeolite 4A, demonstrating that adsorption is ruled by the strong electrostatic interactions with CO_2. Furthermore, an IAST simulation has been carried out and it has been found that the optimal material LTA@Al-BDC could separate a post-combustion mixture with high CO_2/N_2 selectivities (350) at pressures of up to 100 kPa. Besides, the LTA@Al-BDC shows a higher dispersion within a polymeric matrix and a lower water uptake than the bare zeolite, which benefits seeking to produce composite materials for CO_2 separation.

In summary, it has been shown for the first time that a MOF nanosheet shell can be synthesized on an aluminum-rich zeolite core where the aluminum of the MOF comes solely from the zeolite. The zeolite@MOF obtained shows a synergistic behavior of both materials by possessing the CO_2 and H_2 adsorption capacities of the zeolite with the external surface of an organic–inorganic material such as the prepared MOF nanosheets. This reveals the possibility of preparing polymeric composites that can be applied to separation processes as in mixed matrix membranes.

Funding sources

This work gratefully acknowledges grants PID2022-138582OB-I00 and PID2021-123079OB-I00 funded by MICIU/AEI/10.13039/501100011033/ and by “ERDF A way of making Europe”. L. Güemes also thanks the Aragón Government (DGA) for his Ph.D. grant. Financial assistance from the Government of Aragón (T68_23R) is also acknowledged. CEX2023-001286-S funded by MICIU/AEI/10.13039/501100011033/.

CRediT authorship contribution statement

Lucas Güemes: Writing – review & editing, Writing – original draft, Visualization, Validation, Software, Resources, Methodology, Investigation, Formal analysis, Data curation, Conceptualization. **Marta Navarro:** Writing – review & editing, Writing – original draft, Visualization, Validation, Software, Resources, Methodology, Investigation, Formal analysis, Data curation. **Fernando Cacho-Bailo:** Writing – review & editing, Writing – original draft, Methodology, Conceptualization. **Cristian D. Jaimes-Paez:** Writing – review & editing, Writing – original draft, Visualization, Validation, Software, Resources, Methodology, Investigation, Formal analysis, Data curation. **Diego Cazorla-Amorós:** Writing – review & editing, Writing – original draft, Visualization, Validation, Supervision, Resources, Project administration, Methodology, Investigation, Funding acquisition, Formal analysis, Data curation. **Carlos Téllez:** Writing – review & editing, Writing – original draft, Visualization, Validation, Supervision, Resources, Methodology, Investigation, Funding acquisition, Formal analysis, Data curation, Conceptualization. **Joaquín Coronas:** Writing – review & editing, Writing – original draft, Visualization, Validation, Supervision, Resources, Project administration, Methodology, Investigation, Funding acquisition, Formal analysis, Data curation, Conceptualization.

Declaration of competing interest

The authors declare the following financial interests/personal relationships which may be considered as potential competing interests: Fernando Cacho-Bailo is currently employed by the company IQE S.A. The remaining authors declare that the research was conducted in the absence of any commercial or financial relationships that could be construed as a potential conflict of interest.

Acknowledgements

Authors would like to acknowledge the use of Servicio General de Apoyo a la Investigación-SAI, Universidad de Zaragoza. and the use of instrumentation as well as the technical advice provided by the National Facility ELECMI ICTS, node «Laboratorio de Microscopias Avanzadas (LMA)» at «Universidad de Zaragoza».

Appendix A. Supplementary data

Supplementary data to this article can be found online at https://doi.org/10.1016/j.cej.2025.164314.

Data availability

Data will be made available on request.

References

[1] C.S. Cundy, P.A. Cox, The Hydrothermal Synthesis of Zeolites: History and Development from the Earliest Days to the Present Time, Chem Rev 103 (2003) 663–702, https://doi.org/10.1021/cr020060i.

[2] J.W. McBain, The Sorption of Gases and Vapours by Solids, J Phys Chem 37 (1933) 149–150, https://doi.org/10.1021/j150343a021.

[3] A.F. Cronstedt, RÖN och BESKRIFNING Om en oberkant barg art, som kallas Zeolites, Kongl Vetenskaps Academiens Handlingar Stockholm 17 (1756) 120.

[4] S.M. Auerbach, K.A. Carrado, P.K. Dutta, Handbook of zeolite science and technology, CRC Press (2003), https://doi.org/10.1201/9780203911167.

[5] W. Yan, Y. Li, F.-S. Xiao, Z. Liu, J. Yu, The future of zeolites, Chem. Mater. 36 (2024) 7103–7105, https://doi.org/10.1021/acs.chemmater.4c01675.

[6] L.B. Baerlocher, C. Brouwer, D. Marler, B. McCusker, Database of Zeolite Structures, (2017). https://www.iza-structure.org/databases/ (accessed August 27, 2024).

[7] O.M. Yaghi, H. Li, Hydrothermal synthesis of a metal-organic framework containing large rectangular channels, J Am Chem Soc 117 (1995) 10401–10402, https://doi.org/10.1021/ja00146a033.

[8] O.M. Yaghi, G. Li, H. Li, Selective binding and removal of guests in a microporous metal–organic framework, Nature 378 (1995) 703–706, https://doi.org/10.1038/378703a0.

[9] H. Li, M. Eddaoudi, M. O'Keeffe, O.M. Yaghi, Design and synthesis of an exceptionally stable and highly porous metal-organic framework, Nature 402 (1999) 276–279, https://doi.org/10.1038/46248.

[10] V. Valtchev, S. Mintova, Zeolites and MOFs? Dare to Know Them!, in: V. Blay, L.F. Bobadilla, A. Cabrera-García (Eds.), Zeolites and Metal-Organic Frameworks, Amsterdam University Press, 2018: pp. 13–24. https://doi.org/10.2307/j.ctvcmxprm.4.

[11] N. Hanikel, M.S. Prévot, O.M. Yaghi, MOF water harvesters, Nat. Nanotechnol. 15 (2020) 348–355, https://doi.org/10.1038/s41565-020-0673-x.

[12] F. Gao, Y. Li, Z. Bian, J. Hu, H. Liu, Dynamic hydrophobic hindrance effect of zeolite@zeolitic imidazolate framework composites for CO_2 capture in the presence of water, J. Mater. Chem. A Mater. 3 (2015) 8091–8097, https://doi.org/10.1039/C4TA06645F.

[13] F. Yang, J. Wu, X. Zhu, T. Ge, R. Wang, Enhanced stability and hydrophobicity of LiX@ZIF-8 composite synthesized environmental friendly for CO_2 capture in highly humid flue gas, Chem. Eng. J. 410 (2021) 128322, https://doi.org/10.1016/j.cej.2020.128322.

[14] H.L. Choi, Y. Jeong, H. Lee, T.-H. Bae, High-performance mixed-matrix membranes using a zeolite@MOF core–shell structure synthesized via ion-exchange-induced crystallization and post-synthetic conversion, JACS Au 4 (2024) 253–262, https://doi.org/10.1021/jacsau.3c00680.

[15] Y. Zhang, Y. Li, F. Zhang, Y. Wang, J. Li, J. Yang, Insight into construction and growth process of core-shell KCHA@ZIF-8 composites, Microporous Mesoporous Mater. 373 (2024) 113130, https://doi.org/10.1016/j.micromeso.2024.113130.

[16] Q. Al-Naddaf, H. Thakkar, F. Rezaei, Novel zeolite-5A@MOF-74 composite adsorbents with core–shell structure for H_2 purification, ACS Appl. Mater. Interfaces 10 (2018) 29656–29666, https://doi.org/10.1021/acsami.8b10494.

[17] Q. Al-Naddaf, A.A. Rownaghi, F. Rezaei, Multicomponent adsorptive separation of CO_2, CO, CH_4, N_2, and H_2 over core-shell zeolite-5A@MOF-74 composite adsorbents, Chem. Eng. J. 384 (2020) 123251, https://doi.org/10.1016/j.cej.2019.123251.

[18] X. Pan, H. Xu, X. Zhao, H. Zhang, Metal–organic framework-membranized bicomponent core–shell catalyst HZSM-5@UIO-66-NH_2 /Pd for CO_2 selective conversion, ACS Sustain. Chem. Eng. 8 (2020) 1087–1094, https://doi.org/10.1021/acssuschemeng.9b05912.

[19] E.T. Tikue, S.K. Kang, H.J. Ko, S.W. Kim, A.W. Sabir, P.S. Lee, Fabrication of LTA zeolite core and UiO-66 shell structures via surface zeta potential modulation and sequential seeded growth for zeolite/polymer composite membranes, Microporous and Mesoporous, Materials 383 (2025) 113413, https://doi.org/10.1016/j.micromeso.2024.113413.

[20] F. Feyzbar-Khalkhali-Nejad, S.M. Taghavi Kouzehkanan, E. Hassani, B. Hassani, H. Jahromi, S. Adhikari, T.-S. Oh, ZSM-5@MOF-199 core-shell composite adsorbent: rapid ambient synthesis and CO/CO_2 adsorption, Chem. Eng. Sci. 292 (2024) 119969, https://doi.org/10.1016/j.ces.2024.119969.

[21] J. Wu, Y. Zhu, K. Xue, Y. Lu, J. Hu, W. Dai, Efficient elimination of organic contaminants with novel and stable zeolite@MOF layer adsorbents, Particuology 58 (2021) 74–84, https://doi.org/10.1016/j.partic.2021.01.014.

[22] G. Zhu, R. Graver, L. Emdadi, B. Liu, K.Y. Choi, D. Liu, Synthesis of zeolite@ metal–organic framework core–shell particles as bifunctional catalysts, RSC Adv. 4 (2014) 30673, https://doi.org/10.1039/C4RA03129F.

[23] J.J. Pérez Cacho, F. Cacho Bailo, J. Coronas Ceresuela, C. Téllez Ariso, Material Híbrido Poroso Orgánico - Inorgánico, Método de Obtención y Usos, ES2682056, 2018.

[24] J.J. Pérez Cacho, F. Cacho Bailo, J. Coronas Ceresuela, C. Téllez Ariso, Organic-Inorganic porous hybrid material, method for obtaining it and use thereof, EP3595808, 2020.

[25] P. Rani, R. Srivastava, Extra-framework aluminum species of zeolite that surrogate the growth of metal organic framework from zeolite matrix, Chem. Asian J. 14 (2019) 2598–2603, https://doi.org/10.1002/asia.201900612.

[26] C. Zhang, X.S. Lu, A.Z. Gu, How to accurately determine the uptake of hydrogen in carbonaceous materials, Int. J. Hydrogen Energy 29 (2004) 1271–1276, https://doi.org/10.1016/j.ijhydene.2003.12.001.

[27] H.K. Beyer, Dealumination Techniques for Zeolites, in: Post-Synthesis Modification I, Springer Berlin Heidelberg, Berlin, Heidelberg, 2002: pp. 203–255. https://doi.org/10.1007/3-540-69750-0_3.

[28] T. Ruthven, D. Takeguchi, W. Tanakulrungsank, T. Inui, Separation and/or concentration of CO_2 from CO_2/N_2 gaseous mixture by pressure swing adsorption using metal-incorporated microporous crystals with high surface area [Letters to the Editor], Gas Separation & Purification 7 (1993) 3–9, https://doi.org/10.1016/0950-4214(93)85013-L.

[29] W. Fan, K.Y. Wang, C. Welton, L. Feng, X. Wang, X. Liu, Y. Li, Z. Kang, H.C. Zhou, R. Wang, D. Sun, Aluminum metal–organic frameworks: from structures to applications, Coord. Chem. Rev. 489 (2023) 215175, https://doi.org/10.1016/j.ccr.2023.215175.

[30] T. Loiseau, C. Serre, C. Huguenard, G. Fink, F. Taulelle, M. Henry, T. Bataille, G. Férey, A rationale for the large breathing of the porous aluminum terephthalate (MIL-53) upon hydration, Chem. A Eur. J. 10 (2004) 1373–1382, https://doi.org/10.1002/chem.200305413.

[31] C.S. Cundy, P.A. Cox, The hydrothermal synthesis of zeolites: Precursors, intermediates and reaction mechanism, Microporous Mesoporous Mater. 82 (2005) 1–78, https://doi.org/10.1016/j.micromeso.2005.02.016.

[32] M. Sánchez-Sánchez, N. Getachew, K. Díaz, M. Díaz-García, Y. Chebude, I. Díaz, Synthesis of metal–organic frameworks in water at room temperature: salts as linker sources, Green Chem. 17 (2015) 1500–1509, https://doi.org/10.1039/C4GC01861C.

[33] A. Corma, Inorganic solid acids and their use in acid-catalyzed hydrocarbon reactions, Chem. Rev. 95 (1995) 559–614, https://doi.org/10.1021/cr00035a006.

[34] S.M. Campbell, D.M. Bibby, J.M. Coddington, R.F. Howe, Dealumination of HZSM-5 zeolites, J. Catal. 161 (1996) 350–358, https://doi.org/10.1006/jcat.1996.0192.

[35] Y. Oumi, S. Nemoto, S. Nawata, T. Fukushima, T. Teranishi, T. Sano, Effect of the framework structure on the dealumination–realumination behavior of zeolite, Mater. Chem. Phys. 78 (2003) 551–557, https://doi.org/10.1016/S0254-0584(02)00376-0.

[36] A.G. Stepanov, Basics of Solid-State NMR for Application in Zeolite Science, in: Zeolites and Zeolite-Like Materials, Elsevier, 2016: pp. 137–188. https://doi.org/10.1016/B978-0-444-63506-8.00004-5.

[37] J.M. Thomas, C.A. Fyfe, S. Ramdas, J. Klinowski, G.C. Gobbi, High-resolution silicon-29 nuclear magnetic resonance spectrum of zeolite ZK-4: its significance in assessing magic angle spinning nuclear magnetic resonance as a structural tool for aluminosilicates, J. Phys. Chem. 86 (1982) 3061–3064, https://doi.org/10.1021/j100213a003.

[38] M. Dyballa, U. Obenaus, S. Lang, B. Gehring, Y. Traa, H. Koller, M. Hunger, Brønsted sites and structural stabilization effect of acidic low-silica zeolite A prepared by partial ammonium exchange, Microporous Mesoporous Mater. 212 (2015) 110–116, https://doi.org/10.1016/j.micromeso.2015.03.030.

[39] W. Loewenstein, The distribution of aluminum in the tetrahedra of silicates and aluminates, Am. Mineral. 39 (1954) 92–96.

[40] S. Duan, Y. Xie, S. Shen, G. Li, Comparative analysis of CO_2 and N_2 adsorption on zeolite 4A: thermodynamics parameters and site energy distribution investigations, J. Environ. Chem. Eng. 12 (2024) 112870, https://doi.org/10.1016/j.jece.2024.112870.

[41] D.G. Boer, J. Langerak, P.P. Pescarmona, Zeolites as selective adsorbents for CO_2 separation, ACS Appl. Energy Mater. 6 (2023) 2634–2656, https://doi.org/10.1021/acsaem.2c03605.

[42] S. Lowell, J.E. Shields, M.A. Thomas, M. Thommes, Characterization of porous solids and powders: surface area, pore size and density, springer netherlands, Dordrecht (2004), https://doi.org/10.1007/978-1-4020-2303-3.

[43] J. García-Martínez, D. Cazorla-Amorós, A. Linares-Solano, Further evidences of the usefulness of CO_2 adsorption to characterize microporous solids, Stud. Surf. Sci. Catal. 128 (2000) 485–494, https://doi.org/10.1016/S0167-2991(00)80054-3.

[44] M. Thommes, K. Kaneko, A.V. Neimark, J.P. Olivier, F. Rodriguez-Reinoso, J. Rouquerol, K.S.W. Sing, Physisorption of gases, with special reference to the evaluation of surface area and pore size distribution (IUPAC Technical Report), Pure Appl. Chem. 87 (2015) 1051–1069, https://doi.org/10.1515/pac-2014-1117.

[45] K.-J. Hwang, W.-S. Choi, S.-H. Jung, Y.-J. Kwon, S. Hong, C. Choi, J.-W. Lee, W.-G. Shim, Synthesis of zeolitic material from basalt rock and its adsorption properties for carbon dioxide, RSC Adv. 8 (2018) 9524–9529, https://doi.org/10.1039/C8RA00788H.

[46] K.S.W.S. Rouquerol, F. Rouquerol, P. Llewellyn, G. Maurin, Adsorption by Powders and Porous Solids, 2nd ed, Elsevier, San Diego CA USA, 2014. https://doi.org/10.1016/C2010-0-66232-8.

[47] K.-Q. Chang, Y.-H. Dong, K.-Y. Liao, Y.-C. Zeng, Y.-Y. Gou, X.-G. Yi, W. Hui, X.-Y. Xiao, Waste foam to upcycled sponge-like porous carbon composites for efficient CO2 capture and conversion, J. Environ. Chem. Eng. 12 (2024) 112565, https://doi.org/10.1016/j.jece.2024.112565.

[48] F.-F. Mao, Y.-H. Dong, Y. Zhou, M.-S. Sun, W. Hui, D. Tao, Sustainable repurpose of waste melamine foam into bifunctional catalysts for efficient CO2 capture and conversion, Mater. Today Energy 45 (2024) 101677, https://doi.org/10.1016/j.mtener.2024.101677.

[49] L. Shi, K.-Y. Liao, Y.-H. Dong, Y.-A. Wang, Y. Zhou, X.-G. Yi, M.-S. Sun, W. Hui, D.-J. Tao, Hollow branched fiber hierarchical porous carbon as recyclable adsorbents and catalysts for efficient CO2 capture and conversion, Sustain. Mater. Technol. 40 (2024) e00880, https://doi.org/10.1016/j.susmat.2024.e00880.

[50] S. Fujikawa, R. Selyanchyn, T. Kunitake, A new strategy for membrane-based direct air capture, Polym. J. 53 (2021) 111–119, https://doi.org/10.1038/s41428-020-00429-z.

[51] Y.S. Ho, G. McKay, Pseudo-second order model for sorption processes, Process Biochem. 34 (1999) 451–465, https://doi.org/10.1016/S0032-9592(98)00112-5.

[52] M.F. Vega, E. Díaz-Faes, C. Barriocanal, Kinetic and mechanistic study of CO_2 adsorption on activated hydrochars, J. CO_2 Util. 81 (2024) 102716, https://doi.org/10.1016/J.JCOU.2024.102716.

[53] A.L. Myers, J.M. Prausnitz, Thermodynamics of mixed-gas adsorption, AIChE J. 11 (1965) 121–127, https://doi.org/10.1002/aic.690110125.

[54] J. Jia, Y. Wang, Y. Feng, G. Hu, J. Lin, Y. Huang, Y. Zhang, Z. Liu, C. Tang, C. Yu, Hierarchically porous boron nitride/HKUST-1 hybrid materials: synthesis, CO_2 adsorption capacity, and CO_2/N_2 and CO_2/CH_4 selectivity, Ind. Eng. Chem. Res. 60 (2021) 2463–2471, https://doi.org/10.1021/acs.iecr.0c05701.

[55] O. Redlich, D.L. Peterson, A useful adsorption isotherm, J. Phys. Chem. 63 (1959) 1024, https://doi.org/10.1021/j150576a611.

[56] J.M. Kolle, M. Fayaz, A. Sayari, Understanding the effect of water on CO_2 adsorption, Chem. Rev. 121 (2021) 7280–7345, https://doi.org/10.1021/acs.chemrev.0c00762.

[57] L. Martínez-Izquierdo, C. Téllez, J. Coronas, Highly stable Pebax® Renew® thin-film nanocomposite membranes with metal organic framework ZIF-94 and ionic liquid [Bmim][BF_4] for CO_2 capture, J. Mater. Chem. A Mater. 10 (2022) 18822–18833, https://doi.org/10.1039/D2TA03958C.

[58] T.T. Moore, W.J. Koros, Non-ideal effects in organic–inorganic materials for gas separation membranes, J. Mol. Struct. 739 (2005) 87–98, https://doi.org/10.1016/j.molstruc.2004.05.043.